

# Exploring the short-term variability of H $\alpha$ and H $\beta$ emissions in a sample of M dwarfs

Vipin Kumar<sup>1,2,3\*</sup>, A. S. Rajpurohit<sup>1†</sup>, Mudit K. Srivastava<sup>1‡</sup>,  
José G. Fernández-Trincado<sup>4</sup> and A. B. A. Queiroz<sup>5,6,7</sup>

<sup>1</sup>*Astronomy & Astrophysics Division, Physical Research Laboratory, Ahmedabad 380009, India*

<sup>2</sup>*Department of Physics, Indian Institute of Technology, Gandhinagar, 382335, India*

<sup>3</sup>*I. Physikalisches Institut, Universität zu Köln, Zùlpicher Straße 77, 50937, Köln, Germany*

<sup>4</sup>*Instituto de Astronomía, Universidad Católica del Norte, Av. Angamos 0610, Antofagasta, Chile*

<sup>5</sup>*Leibniz-Institut für Astrophysik Potsdam (AIP), An der Sternwarte 16, 14482 Potsdam, Germany*

<sup>6</sup>*Institut für Physik und Astronomie, Universität Potsdam, Haus 28 Karl-Liebknecht-Str. 24/25, D-14476 Golm, Germany*

<sup>7</sup>*Laboratório Interinstitucional de e-Astronomia - LIneA, Rua Gal. José Cristino 77, Rio de Janeiro, RJ - 20921-400, Brazil*

Accepted YYYY Month DD. Received YYYY Month DD; in original form YYYY Month DD

## ABSTRACT

The time scales of variability in active M dwarfs can be related to their various physical parameters. Thus, it is important to understand such variability to decipher the physics of these objects. In this study, we have performed the low resolution ( $\sim 5.7$  Å) spectroscopic monitoring of 83 M dwarfs (M0-M6.5) to study the variability of H $\alpha$  / H $\beta$  emissions; over the time scales from  $\sim 0.7$  to 2.3 hours with a cadence of  $\sim 3$ -10 minutes. Data of a sample of another 43 late-type M dwarfs (M3.5-M8.5) from the literature are also included to explore the entire spectral sequence. 53 of the objects in our sample ( $\sim 64\%$ ) show statistically significant short-term variability in H $\alpha$ . We show that this variability in 38 of them are most likely to be related to the flaring events. We find that the early M dwarfs are less variable despite showing higher activity strengths ( $L_{H\alpha}/L_{bol}$  &  $L_{H\beta}/L_{bol}$ ), which saturates around  $\sim 10^{-3.8}$  for M0-M4 types. Using archival photometric light curves from TESS and Kepler/K2 missions, the derived chromospheric emission (H $\alpha$  and H $\beta$  emission) variability is then explored for any plausible systematics with respect to their rotation phase. The variability indicators clearly show higher variability in late-type M dwarfs (M5-M8.5) with shorter rotation periods ( $< 2$  days). For 44 sources, their age has been estimated using StarHorse project and possible correlations with variability have been explored. The possible causes and implications for these behaviors are discussed.

**Key words:** stars: activity - stars: flare - stars: late-type - stars: magnetic fields

## 1 INTRODUCTION

M dwarfs are the major stellar constituents of the Galaxy. Their population is estimated to be nearly  $\sim 70\%$  of the total stellar content in our Galaxy, and they contribute  $\sim 40\%$  of its total stellar mass (Henry et al. 1997; Chabrier 2003). M dwarfs are less massive ( $0.6$ - $0.075 M_{\odot}$ ) and cooler stars with effective temperature ( $T_{\text{eff}}$ ) in the range of  $2500$ - $4000$  K. As their mean lifetimes on the main sequence path are comparatively much longer, they are a good tracer of the Galactic history (Green & Margon 1994; Cool et al. 1996;

Renzini et al. 1996). A variety of them are expected to host sub-stellar objects, e.g., brown dwarfs and exoplanets, (Boufils et al. 2012; Gillon et al. 2017; Mercer & Stamatellos 2020; Baroch et al. 2021), therefore they have been a major topic of attention in recent times.

It is well established that magnetic fields are the sole reason for stellar magnetic activity and almost certainly play a fundamental role in the physics of late-type stellar atmospheres. A large fraction of M dwarfs are known to be magnetically active (West et al. 2008, 2015). It is expected that  $30$ - $40\%$  of M dwarfs are members of stellar or sub-stellar binary systems. Interactions between M dwarfs and their binary companion may impact the companion's evolution due to the activity of the M dwarf as suggested by Kouwenhoven et al. (2009) and Dressing & Charbonneau (2015).

\*kumar@ph1.uni-koeln.de

†arvindr@prl.res.in

‡mudit@prl.res.in

M dwarfs with masses below  $0.35M_{\odot}$  (Chabrier & Baraffe 1997), become fully convective and, unlike solar-type stars, lack the tachocline region, which is thought to be essential for their magnetic field generation. In such fully convective M dwarfs, the mechanisms for generating large-scale magnetic fields are not yet well understood (Newton et al. 2017). Therefore, a thorough understanding of the M dwarf magnetic activity is essential to explore various physical processes associated with its generation.

Observable phenomena produced in the outer stellar atmosphere, such as strong stellar winds, flares, coronal mass ejection, spots, etc., are used to describe the level of magnetic activity in stars. The magnetic heating of the stellar atmosphere results in various chromospheric emissions such as *Ca II* H+K, *Na I* D, *Mg II* and *K* along with  $H\alpha$  are commonly used as a proxy of magnetic activity in M dwarfs (Hawley et al. 1996; Lee et al. 2010; Fuhrmeister et al. 2019; Schöfer et al. 2019). Out of these, the chromospheric  $H\alpha$  emission line is widely used for activity-related studies, as it is easily observable in M dwarfs compared to other lines in the faint blue part of the spectrum (Walkowicz & Hawley 2009). Because of magnetic activity, these atomic lines can be affected by line profile changes which are thought to be caused by star spots or plages (Schöfer et al. 2019).

Magnetic activity indicators, such as  $H\alpha$  emission in the chromosphere, and X-ray emissions in the corona, is measurable evidence of their surface magnetism. Studies by Angus et al. (2015); West et al. (2008); Mamajek & Hillenbrand (2008); Reiners et al. (2012); Newton et al. (2017); Riedel et al. (2017); Kiman et al. (2019) and Kiman et al. (2021) show that magnetic activity is known to be correlated with stellar age. These magnetic activity are partly responsible for the stellar magnetic wind, which dissipates angular momentum, and appears to scale with stellar rotation. Thus magnetic activity and age are tightly related for solar-type stars (Mamajek & Hillenbrand 2008). Furthermore, Reiners et al. (2012), West et al. (2015), Newton et al. (2017), and Riedel et al. (2017) find that in M dwarfs, the magnetic activity decreases with age for late-M dwarfs though, for fully convective M dwarfs, the mechanism to generate magnetic fields is not yet well understood.

The tracers of magnetic activity are also closely tied to stellar rotation in solar-type stars and become stronger for stars, which rotate faster (Pallavicini et al. 1981; Wright et al. 2011; Reiners et al. 2014). The stellar rotation period can be determined with various spectroscopic and photometric measurements. Suárez Mascareño et al. (2018), and Fuhrmeister et al. (2019) measured the rotation periods of early M dwarfs using spectroscopic indicators such as  $H\alpha$ , *Ca II* H+K, or *K* where the inhomogeneous distributions of stellar surface features lead to variations over the course of its rotation. While Kiraga & Stepien (2007); Irwin et al. (2011); Newton et al. (2016, 2018) measured the rotation periods for M dwarfs using photometry by measuring the brightness variations caused by long-lived star spots.

A strong correlation between rotation period and magnetic activity is found for early-type M dwarfs (masses  $>0.35M_{\odot}$ ) (Reiners et al. 2012; West et al. 2015; Newton et al. 2017). M dwarfs earlier than M3 show a clear saturated rotation-activity relationship as demonstrated in coronal X-ray emission (Wright et al. 2011), and  $H\alpha$ , *Ca II* H+K emission in the chromosphere. Recently, Wright et al. (2018) finds

that fully convective M dwarfs (masses  $<0.35M_{\odot}$ ) also follow the same X-ray rotation–activity relationship. Further, Newton et al. (2017) suggested that depending on the mass, M dwarfs with spectral type earlier than M2.5 shows an increment in  $H\alpha$  activity with a decreasing period and reaches a saturated level for Rossby numbers (a quantity which describes the strength of the rotational effect on the convective flows) smaller than  $\sim 0.1$  and start to decline after  $R_0 > 0.2$ .

West et al. (2015) shows that in M dwarfs, the activity fraction decreases with increasing rotation period for early-type M dwarfs (M1-M4), whereas the higher activity fraction for late-type M dwarfs extends to slower rotation rates. Similarly, Jenkins et al. (2009) finds the change in the rotation period at the fully convective boundary. They attribute this to the changing field topology between partially and fully convective stars as suggested by (Reiners & Basri 2007). However, with similar rotation periods and masses in fully convective M dwarfs, Morin et al. (2010) found that magnetic field topologies fall largely into two categories: one group has strong, axisymmetric, largely dipolar global fields, while the other group showed weak, non-axisymmetric global fields.

In recent times, TESS and Kepler/K2 missions (Caldwell et al. 2010; Koch et al. 2010; Howell et al. 2014; Ricker et al. 2015) have offered another opportunity to study various activity indicators, e.g., star-spots, bright faculae, etc. The high cadence data from these missions are successfully used to explore the short-duration activity in the photometry light curves (Doyle et al. 2018, 2019). The modulation in the photometric light curve originates due to the presence of starspots/bright faculae on the stellar surface (Radick et al. 1998; Hall et al. 2009; Buccino et al. 2011). Thus the correlations/anti-correlation of any activity indicator strength (such as  $H\alpha$  emission) with the rotation phase have also been examined in the context of emission originating from such star spots and/or bright faculae. Such previous studies e.g., Radick et al. (1998); Hall et al. (2009); Buccino et al. (2011); Medina et al. (2022) indicate that some M dwarfs show a correlation/anti-correlation between chromospheric emission strength with the rotation phase. i.e., the emission strength increases with the increase/decrease in brightness of the star (caused by the rotation of the star).

The magnetic activity in the M dwarf happens at various time scales ranging from a few seconds to several hours (Kowalski et al. 2010; Yang et al. 2017). Doyle et al. (2018, 2019) demonstrated that magnetic activity and energetic flaring events on the stellar surface could vanish in seconds to hours. Such activity would then invariably be seen in the flux variation in  $H\alpha$  (Lee et al. 2010; Hilton et al. 2010; Almeida et al. 2011; Walkowicz et al. 2011; Hawley et al. 2014; Chang et al. 2017). While a good sample of M dwarfs has been studied to characterise the activity at the larger time scales through  $H\alpha$  variability, very few studies in the literature investigate  $H\alpha$  variability at shorter time scales of a few minutes (for e.g., 5-20 minutes and/or with a sample of uneven cadence). Thus, short-duration behaviour could not be probed, leading to a gap in the systematic understanding of  $H\alpha$  variability on such time scales.

One such short-scale systematic data set was presented by Lee et al. (2010), who had studied 43 sources of M3.5-M8.5 spectral range at a cadence of  $\sim 5$  to 10 minutes over a timescale of  $\sim 0.1$ -1 hr. Though later Kruse et al. (2010) had

expanded this study over a complete spectral sequence (M0-M9), they mostly used SDSS survey data of longer exposure time ( $\sim 15$  minutes). Recently, [Medina et al. \(2022\)](#) used high-cadence spectroscopic data to examine  $H\alpha$  variability on the timescales of minutes to hours on a sample of 13 fully convective, active mid-to-late M stars. Their study concludes that the dominant source of  $H\alpha$  variability on the timescales could be the low-energy flares.

Therefore, in this study, we have performed a systematic short-term (mostly 5 minutes individual frame exposures over 0.7-2.3 hours) spectroscopy monitoring of a sample of M dwarfs in the spectral range of M0-M6.5 to probe their  $H\alpha$  variability. This chosen spectral range was apt as our sample of 83 M dwarfs in M0-M6.5 spectral class complemented the data set provided by [Lee et al. \(2010\)](#) in the range of M3.5-M8.5. We have, thus, constructed a sample of  $\sim 126$  sources in the complete spectral range of M0-M8.5.

The outline of this paper is as follows. In Section 2, we have described the sample selection criteria and observations. In Section 3, we have discussed the results from our spectroscopic analysis, like the estimation of atmospheric parameters,  $H\alpha$  and  $H\beta$  variability indicators, activity strength measurements, etc. In Section 4, we have estimated the rotation periods and star-spot filling factor with the help of photometric light curves and relate these rotation periods with the variability indicators. In Section 5, we have derived the age of the sources using StarHorse project and discussed observed variability with their age. Finally, we summarized our results and discussed the implications in Section 6.

## 2 SAMPLE SELECTION & OBSERVATIONS

For this observing campaign, we targeted the M dwarfs in the spectral range M0-M6.5 with MFOSC-P instrument on the PRL 1.2 m, f/13 telescope ([Srivastava et al. 2018, 2021; Rajpurohit et al. 2020](#)). The moderate aperture of the telescope and cumulative (telescope + instrument) efficiency compelled us to restrict our sample with V magnitude brighter than 14 typically. This also restricts us from expanding our spectral range beyond M6 as most of the late M dwarf (M7 and beyond) are fainter ( $V > 16$ ) for spectroscopy with MFOSC-P on 1.2m telescope. The distribution of all the sources is shown in Fig. 1. The selected sources in this study have typical  $H\alpha$  equivalent widths (EW)  $< -0.75 \text{ \AA}$ , which usually corresponds to the detectable  $H\alpha$  line in emission. Thus, we selected 83 suitable targets from the list of [Jeffers et al. \(2018\)](#) and [Lépine & Gaidos \(2011\)](#). They were observed between March 2020 to March 2021. The details of these targets are summarized in Table 1.

The instrument MFOSC-P (Mount-Abu Faint Object Spectrograph and Camera-Pathfinder) is an imager-spectrograph ([Srivastava et al. 2018, 2021](#)) which provides visible-band spectroscopy using three plane reflection gratings of 600, 300, and 150 line-pairs(lp)  $\text{mm}^{-1}$ . These gratings offer resolutions of  $R \sim 2000, 1000$  and 500 centered at  $\sim 6500, 5500, 6000 \text{ \AA}$  and are referred to as R2000, R1000, and R500 modes, respectively. For the current observing program, we have utilized R1000 mode (300 lp  $\text{mm}^{-1}$ , dispersion  $\sim 1.9 \text{ \AA}$  per pixel) with 1 arc-second ( $\sim 3$  pixels) slit-width covering a spectral range of 4700-6650  $\text{ \AA}$ , i.e., covering both  $H\beta$  and  $H\alpha$  wavelengths. The targets were monitored with integra-

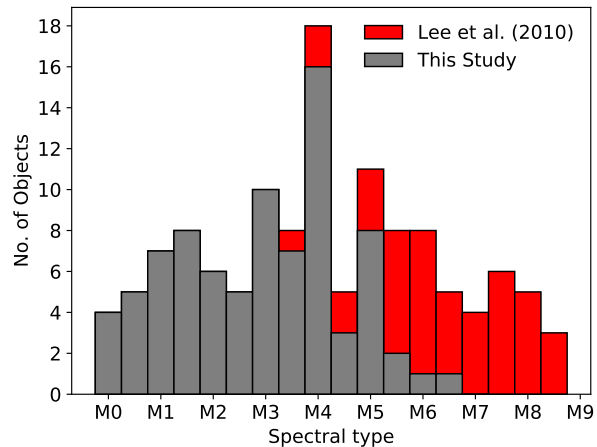


**Figure 1.** Distribution of 83 M dwarfs of this study along with 43 M dwarfs from [Lee et al. \(2010\)](#) with respect to the spectral type.

tion times in the range of 200-600s per frame for  $\sim 0.7$ -2.3 hours in a single stretch for each of the sources. Thus, each data set consists of typically  $\sim 8$ -18 frames of the individual spectrum. A lower-resolution spectrum was also recorded for each of the sources in R500 mode (150 lp  $\text{mm}^{-1}$ , dispersion  $\sim 3.8 \text{ \AA}$  per pixel) to cover a larger wavelength range  $\sim 4500$ -8500  $\text{ \AA}$  for spectral classification purposes. Xenon lamp spectra for wavelength calibration were obtained at the beginning/end of each spectral time series in the identical settings of the instrument. Spectro-photometric standard stars from the ESO catalog <sup>1</sup> were observed (on the same or contemporaneous nights) in the identical setting of the instrument to correct the instrument response. Subsequently, the standard MFOSC-P data reduction procedure has been applied to produce the science-ready spectra (see [Rajpurohit et al. \(2020\)](#) for details). The log of the MFOSC-P spectroscopy are given in Table 1. Photometric light curves of 75 of the above sources were obtained from the TESS and Kepler/K2 archival databases through Mikulski Archive for Space Telescopes (MAST) portal<sup>2</sup>. The related analysis and derived results are discussed in Section 4.

## 3 ANALYSIS AND RESULTS FROM SPECTROSCOPY

### 3.1 Determination of Atmospheric Parameters and Spectral Class

Though the spectral classification of the targets is given in [Lépine et al. \(2013\)](#) and [Jeffers et al. \(2018\)](#), we nevertheless choose to re-confirm those with MFOSC-P low resolution (R500 mode) spectra. Even though the second-order contamination (beyond 7600  $\text{ \AA}$ ) is expected to be minimal given the low U- to I-band flux ratios for M dwarfs (as well as the low spectral throughput of the instrument + telescope in the bluer part), we have restricted the spectral range to 4500-7500  $\text{ \AA}$  for this purpose. The spectral classification was

<sup>1</sup> <https://www.eso.org/sci/observing/tools/standards/spectra/stanlis.html>

<sup>2</sup> <https://mast.stsci.edu/portal/Mashup/Clients/Mast/Portal.html>

derived by comparing the spectra with M dwarf templates from [Bochanski et al. \(2007\)](#) using a similar approach as adopted in [Rajpurohit et al. \(2020\)](#). The derived spectral classes are in good agreement with the spectral classes given by [Lépine et al. \(2013\)](#), and [Jeffers et al. \(2018\)](#) within one spectral class. In this work, however, we shall be using the spectral classes of [Lépine et al. \(2013\)](#), and [Jeffers et al. \(2018\)](#) as they were derived with higher resolution spectra. The spectral classes for six sources were not available in these references. Thus, we took their values from our analysis.

To derive the atmospheric parameters  $T_{\text{eff}}$ , surface gravity ( $\log g$ ), the observed spectra ( $R \sim 500$ ) were compared with the BT-Sett synthetic spectra ([Allard et al. 2010, 2013; Rajpurohit et al. 2012](#)), similar to the approach adopted in [Rajpurohit et al. \(2020\)](#). The grid for  $T_{\text{eff}}$  spans between 3000 to 4000 K in steps of 100 K, and  $\log g$  ranges from 4.0 to 5.5 in steps of 0.5 dex has been used for the comparison. Similar to [Rajpurohit et al. \(2020\)](#), the grid at solar metallicity is used as the sources in this study also lies within 100 pc of the solar neighborhood. In [Fig. 2](#), we show one such comparison of the observed spectra with the synthetic ones for the spectral range M0-M6.5. The spectral range between 5000 to 7500 Å has been used for the  $\chi^2$  minimization. The spectral regions between 6540-6585 Å and 6840-6920 Å (containing H $\alpha$  and H $\beta$  emission line and telluric feature, respectively) were excluded for this analysis. The parameters derived would, thus, have errors equal to the grid spacing, i.e., 100 K for  $T_{\text{eff}}$  and 0.5 dex for  $\log g$ . The derived atmospheric parameters of all the sources are summarized in [Table 1](#) along with the observing log.

### 3.2 H $\alpha$ & H $\beta$ Equivalent widths and their variability

The EWs of H $\alpha$  and H $\beta$  emissions are calculated as,

$$EW = \sum \left( 1 - \frac{F(\lambda)}{F_c(\lambda)} \right) \delta\lambda \quad (1)$$

where  $F(\lambda)$  &  $F_c(\lambda)$  are the line and continuum flux at wavelength  $\lambda$  respectively, and  $\delta\lambda$  is the pixel size in the unit of wavelength. The errors in EWs include the errors in the line and continuum fluxes and errors in wavelength calibration. Following [Hilton et al. \(2010\)](#), the spectral wavebands for the H $\alpha$  and H $\beta$  are 6557.6-6571.6 Å and 4855.7-4870.0 Å respectively. The corresponding continuum regions are 6500-6550 Å & 6575-6625 Å for H $\alpha$  and 4810-4850 Å & 4880-4900 Å for H $\beta$  emissions. The average values of the continuum flux in these regions are chosen for the EWs estimations while summing the area under the line.

As discussed in [Section 2](#), each of our sources typically has 8-18 numbers of individual spectral frames with exposure time per frame in the range of 200-600s, depending on source brightness. To quantify the emission line flux variability in this time series, a  $\chi^2$  minimization is performed over the EW time series (EW light-curve) for each source. The  $\chi^2$  values have been estimated by fitting a straight line at a constant EW to H $\alpha$  and H $\beta$  EW light curves. The confidence of  $\chi^2$  fit was determined by calculating  $p$ -values for given degrees of freedom, using an open-source numerical library

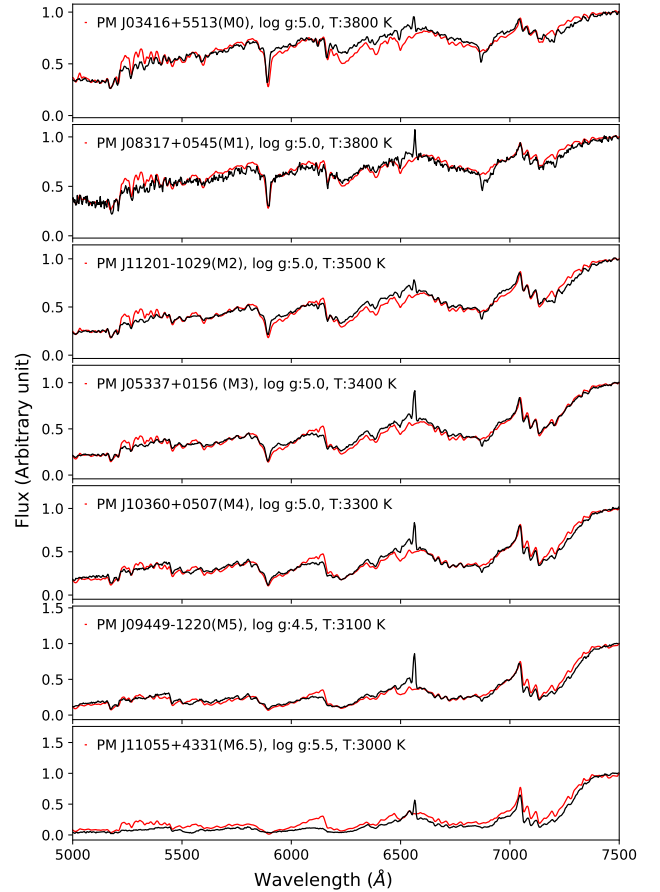


**Figure 2.** Comparison of observed spectra of M dwarfs (black) at  $R \sim 500$  with the best-fit BT-Settl synthetic spectra (red).

`scipy.stats.chi2`<sup>3</sup> of Python. A source is termed as a variable if its  $p$ -value was determined to be less than 0.05. In our sample of 83 M dwarfs, we find that 30 objects ( $\sim 36\%$ ) show no variation in the H $\alpha$  emission with the confidence level more than 95% ( $p$ -value  $< 0.05$ ). The computed  $p$ -value of each source is listed in [Table 2](#) for both H $\alpha$  and H $\beta$  time series. The summary of the median ( $\langle EW \rangle$ ), minimum (Min), maximum (Max), and root-mean-square (RMS) values of the H $\alpha$  & H $\beta$  EWs are also given in [Table 2](#).

We use the same metrics to quantify the variability strength as used by [Lee et al. \(2010\)](#), namely,  $\Delta EW = \text{Max}(EW) - \text{Min}(EW)$ ,  $\text{RMS}(EW)/\langle EW \rangle$  and  $R(EW) = \text{Max}(EW)/\text{Min}(EW)$  for both the H $\alpha$  and H $\beta$  emission lines. This helps in comparing the variability observed in our sample in the range of M0-M6.5 with that of [Lee et al. \(2010\)](#) in the M3.5-M8.5 spectral range. Further, these quantities do not require normalization by  $L_{\text{bol}}$  for comparison across spectral types ([Kruse et al. 2010](#)). In [Fig. 3](#), we show the variations of these quantities as a function of spectral types (panels a, b, c for H $\alpha$  and panels e, f, g for H $\beta$ ). As reported earlier by [Lee et al. \(2010\); Kruse et al. \(2010\)](#), we notice a clear rising trend, which signifies the higher activity in the later types of M dwarfs. Panels (d) and (h) in [Fig. 3](#) show the distribution of median normalized RMS values of

<sup>3</sup> <https://docs.scipy.org/doc/scipy/reference/generated/scipy.stats.chi2.html>

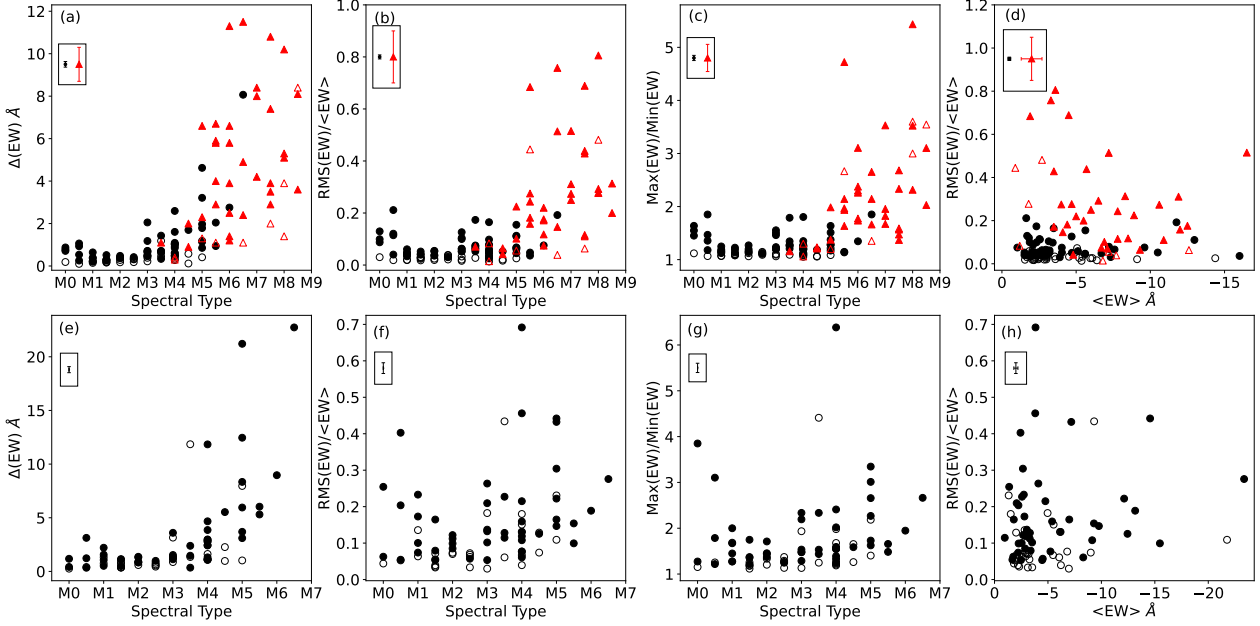


**Figure 3.** Plots showing the variations of various quantities depicting the variability of the EWs of  $H\alpha$  and  $H\beta$  emissions in  $M$  dwarfs. Panels (a), (b), and (c) (in the top row for  $H\alpha$ ) and panels (e), (f) and (g) (in the bottom row for  $H\beta$ ) show the changes in  $\Delta(\text{EW})$ ,  $\text{RMS}(\text{EW})/\langle \text{EW} \rangle$ , and  $\text{Max}(\text{EW})/\text{Min}(\text{EW})$  respectively as the function of spectral type. Panels (d) and (h) show the variation of  $\text{RMS}(\text{EW})/\langle \text{EW} \rangle$  with respect to  $\langle \text{EW} \rangle$  for  $H\alpha$  and  $H\beta$  respectively. Black circles represent the data points of our sample in this study. Red triangles represent the data points derived from the values given in Table-2 of Lee et al. (2010). Filled and open circles/triangles represent the objects identified with varying and non-varying  $H\alpha$  using the  $\chi^2$  criterion ( $p < 0.05$  for variable sources). The error bars in the box on the top-left corner show the median errors of the data points. See Section 3.2 for more details.

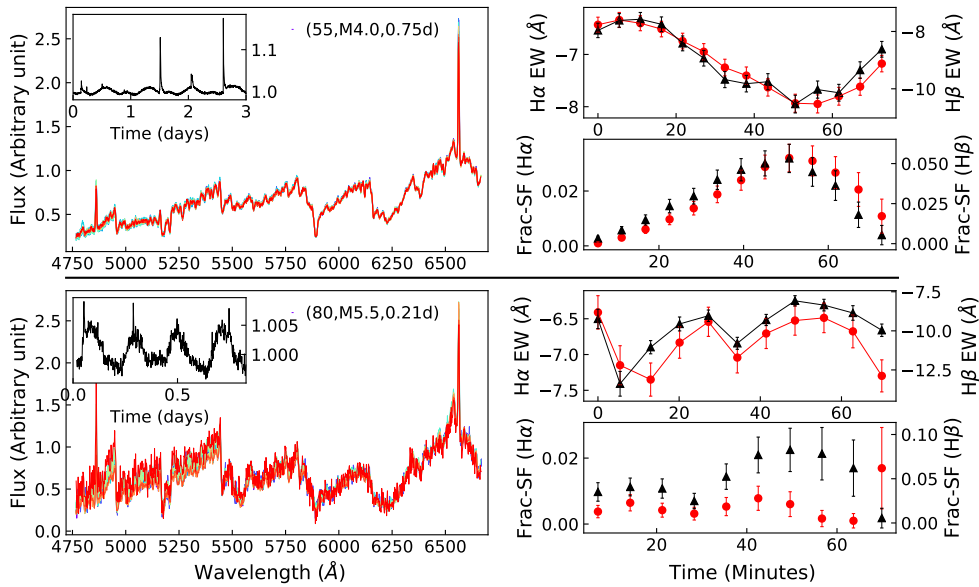


**Figure 4.** The figure shows the time-varying spectra of two sources (source ID: 55 in the top panel and Source ID: 80 in the bottom panel) along with their photometric light curves in the inset. Source ID, spectral type, and rotation period are also mentioned in each of the panels. The corresponding upper and bottom right side panels show the time variations of the EWs of  $H\alpha$  /  $H\beta$  and fraction structure function (SF), respectively. Data for  $H\alpha$  and  $H\beta$  are shown in red circles and black triangles, respectively. See Section 3.2 for discussion. Similar plots for all the sources of this study are given as Appendix-I in the supplementary material.

**Table 1.** Observation details of the sources of this study along with the derived stellar parameters. V band magnitudes are taken from the SIMBAD database. The spectral types are mostly taken from [Lépine et al. \(2013\)](#), and [Jeffers et al. \(2018\)](#), except for six sources where we have derived the spectral class. These sources are marked with (\*). The full table for all the sources is given in Table-1 of Appendix-III in the supplementary material.

Source ID	Source name	Spectral type	Magnitude (V-band)	Date of observation (UT)	Frame exposure time × No. of frames (s)	log g (cm s <sup>-2</sup> )	T <sub>eff</sub> (K)
1	PM J03332+4615S	M0.0	13.09	2020-12-29.602	300sx14	5.0	3900
2	PM J03416+5513	M0.0	-	2021-02-01.600	300sx18	5.0	3800
3	PM J07151+1555	M0.0	11.37	2021-01-30.754	300sx18	5.0	4000
--	--	--	--	--	--	--	--

EWs (RMS(EW) / ⟨EW⟩) with respect to ⟨EW⟩, for H $\alpha$  and H $\beta$  respectively. Here the segregation of our data set (M0-M6.5) and [Lee et al. \(2010\)](#) (M3.5-M8.5) data set is more prominent. The later types of M dwarfs, though having lesser ⟨EW⟩, tend to be more variable. The values of RMS(EW)/⟨EW⟩ for our sources (M0-M6.5) are found to be below  $\sim 0.2$  for H $\alpha$  and below  $\sim 0.5$  for H $\beta$ . These trends are again discussed in Section 6 along with other results.

We attempted to explore the time scales of this variability, if any, using a simple construct of the fractional structure function (SF). For a given EW time series (for H $\alpha$  and H $\beta$ ), the fractional SF at a given time scale ( $\tau$ ) is defined as,

$$SF(\tau) = \left\langle \left[ \frac{EW(t+\tau) - EW(t)}{\text{Mean}(EW)} \right]^2 \right\rangle \quad (2)$$

where  $EW(t+\tau)$  and  $EW(t)$  are two measurements of EW at the time interval of  $\tau$  and  $\text{Mean}(EW)$  is the mean value of the EWs in the full-time series. The time interval values ( $\tau$ ) have been chosen so that they will start with the minimum time interval to the maximum time intervals present in the EW series. The spectra, EW light curves, and fractional SFs for H $\alpha$  and H $\beta$  are shown in Fig. 4 for two of the sources of our sample. Similar plots for all the sources of our sample are given in Appendix-I in the supplementary material. Though the fractional SFs do not clearly show any characteristic time scale of variability (especially at lower times of a few minutes), they nevertheless reinforce an interesting trend noticed by [Bell et al. \(2012\)](#).

The sources which are seen to be varied at a longer time scale (e.g., source ID: 55 in the upper panel of Fig. 4) exhibit a fractional SF, which shows an increasing trend, as expected. However, conforming to the results of [Bell et al. \(2012\)](#), the sources whose EWs light curves are seen to be varied at shorter time scales (e.g., source ID: 80 in the lower panel of Fig. 4) show a nearly flat distribution of fractional SF at all times. [Bell et al. \(2012\)](#) attributed such behavior of the highly variable sources due to the variability time scale shorter than their smallest time-separation bin of  $\sim 15$  minutes. We also see the same trend even at the cadence of  $\sim 5$  minutes.

In order to explore the time scale of variability for a particular spectral type (e.g., M0, M1, etc.) in our sample, we first calculated the normalized-structure function at time scale ( $\tau$ ) as,

$$\text{Normalized } SF(\tau) = \left[ \frac{EW(t+\tau) - EW(t)}{\text{Mean}(EW(t+\tau), EW(t))} \right]^2 \quad (3)$$

This was done for all the EW time series (for all the sources in that particular spectral bin). Later the cumulative-

normalized structure function (CNSF) at time scale  $\tau$  is calculated by taking the mean of these normalized structure functions. We show the cumulative normalized structure function for different spectral bins of our sources in Fig. 5. While a peak is seen in these plots for the early type M dwarfs (M0-M2), signifying the presence of a variability time scale ( $\sim 40$ -60 minutes) in the H $\alpha$  EW, this behavior is not very obvious in the mid-type M dwarfs (M3 and M4), thereby indicating that possibly the time scale of variability is longer than 60 minutes. For M5, it might have two peaks showing  $\sim 30$  minutes of variability time scale or having a significant peak at a longer time scale, thus longer monitoring is required to confirm the variability time scales. These variability time scales conform with the reported value (0.25 - 1 hour) in the other studies e.g., [Lee et al. \(2010\)](#); [Kruse et al. \(2010\)](#); [Bell et al. \(2012\)](#). Though we could only observe different time scales of variability for early to mid M dwarfs, a similar result is also presented by [Kruse et al. \(2010\)](#), who mentioned that the time scale of variability increases with later spectral types. We suggest that such differences in the time scales of variability could be due to different magnitudes of magnetic activity as a function of spectral type.

### 3.3 H $\alpha$ and H $\beta$ activity strength and flaring sources

H $\alpha$  or H $\beta$  activity strength is defined as the ratio of their luminosity to the bolometric luminosity ([West et al. 2008](#); [Hilton et al. 2010](#); [Lee et al. 2010](#); [Newton et al. 2017](#)). The activity strength enables a better comparison of activity between stars of different masses than EW alone ([Reid et al. 1995](#)), as it shows the importance of the line flux relative to the entire energy output of the star. We adopted the following relations given by [Douglas et al. \(2014\)](#) to calculate the H $\alpha$  and H $\beta$  activity strength as,

$$\begin{aligned} \frac{L_{H\alpha}}{L_{bol}} &= -\chi_{H\alpha} \times (EW)_{H\alpha} \\ \frac{L_{H\beta}}{L_{bol}} &= -\chi_{H\beta} \times (EW)_{H\beta} \end{aligned} \quad (4)$$

where  $EW_{H\alpha}$  and  $EW_{H\beta}$  are the equivalent widths of the H $\alpha$  and H $\beta$  emission lines respectively, and the  $\chi$  factor for H $\alpha$  and H $\beta$  are derived from photometric color ( $i - J$ ) ([Walkowicz et al. 2004](#); [Douglas et al. 2014](#); [West & Hawley 2008](#)). The  $\chi$  factor is defined as the ratio of the flux in the continuum near H $\alpha$  to the bolometric flux ([Walkowicz et al. 2004](#)). For the sources where  $i$  magnitudes are not available, we adopted the approach of [Newton et al. \(2017\)](#) first to calculate the  $M_{Earth}$  magnitudes ([Dittmann et al. 2016](#)) and

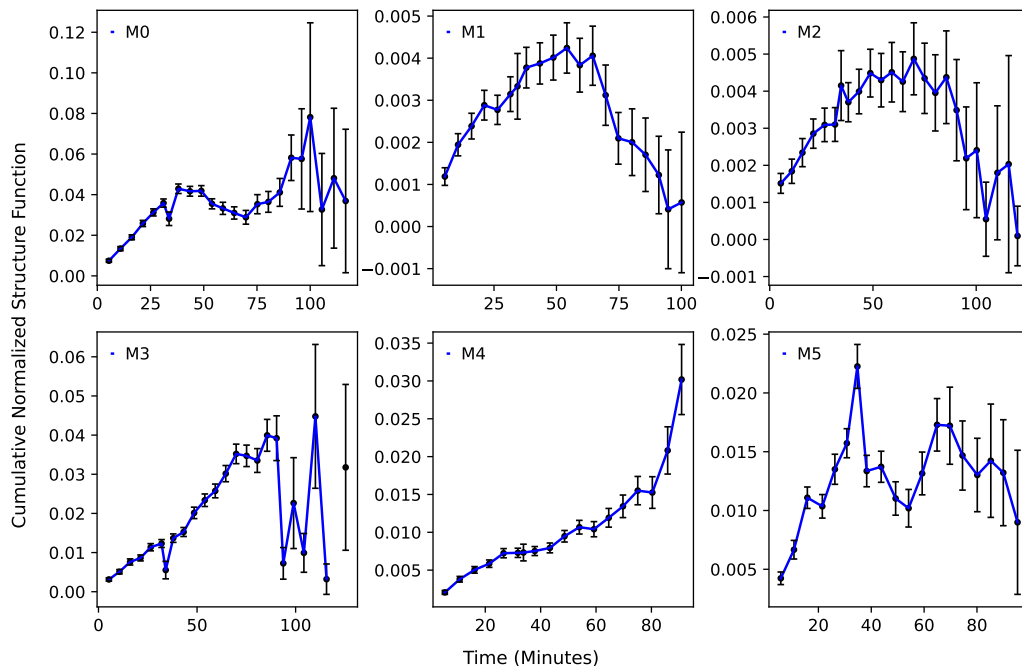


**Figure 5.** The figure shows the cumulative normalized structure function for various spectral classes for sources observed in this study.

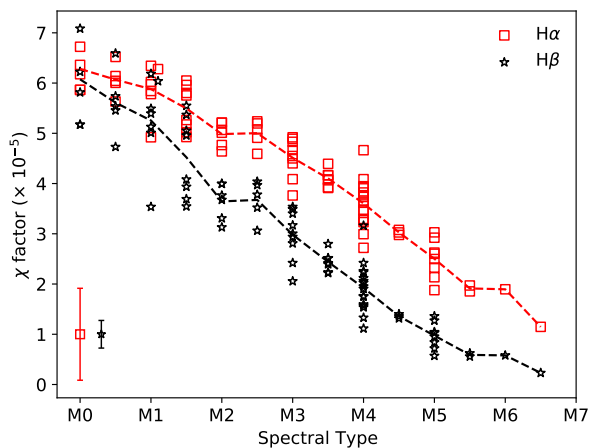


**Figure 6.** The derived  $\chi$  factors for  $H\alpha$  and  $H\beta$  are shown with respect to spectral types. Median error bars are shown in the bottom-left of the plot. The lines joining the mean values of  $\chi$  factors for a given spectral bin are also shown for  $H\alpha$  and  $H\beta$ .

later applied the relation given in Section 3.3 in [Newton et al. \(2017\)](#) to calculate the final  $i_{48} - J$  color. Similar to [Newton et al. \(2017\)](#), we have not made any additional correction between  $i_{48}$  and  $i$  as it would be minor. In Fig. 6, we show the variation of derived  $\chi$  factors as a function of the spectral type where a trend similar to [Newton et al. \(2017\)](#) is noticed. They are also consistent with the range of  $\chi$  factors given in [Newton et al. \(2017\)](#).

The derived values of the means of  $L_{H\alpha}/L_{bol}$  and  $L_{H\beta}/L_{bol}$  are shown in Fig. 7 (top-right panel for  $H\alpha$  and bottom-right panel for  $H\beta$ ) with respect to their spectral

type. The ratio of maximum to minimum values of these quantities (for  $H\alpha$  and  $H\beta$ ) to their mean value is shown in the top-left and bottom-left panels of Fig. 7. Both of these,  $L_{H\alpha}/L_{bol}$  and  $L_{H\beta}/L_{bol}$ , represents the activity strength of the M dwarfs. The plots for  $H\alpha$  also include the values from Table-2 of [Lee et al. \(2010\)](#) as well. It is to be noted that [Lee et al. \(2010\)](#) did not provide the values of  $L_{H\alpha, min}/L_{bol}$ . Therefore we have first calculated the  $\chi$  factor using  $L_{H\alpha, max}/L_{bol}$ , and the corresponding value of maximum EW (using equation 4). This  $\chi$  factor was then used with the corresponding value of minimum EW (from Table-2 of [Lee et al. \(2010\)](#)) to calculate the value of  $L_{H\alpha, min}/L_{bol}$ .

$L_{H\alpha}/L_{bol}$  reaches a constant value of  $\sim 10^{-3.8}$  for the M dwarfs with spectral type M0-M4 and then declines for later spectral types (later than M4), indicating the lower activity strengths for the later types. However, the variability, which can be estimated as the ratio of maximum to minimum values (of the  $H\alpha$  and  $H\beta$  line flux for a given time series of an M dwarf), is higher for these later spectral types. This again signifies that though the strength of the activity in these late-type M dwarfs is low, they are more variable.

Though  $H\alpha$  in M dwarfs is known to show variability up to 30% in the “quiescent” phase ([Gizis et al. 2002](#); [Hilton et al. 2010](#); [Lee et al. 2010](#)), flaring events during the observing window could also cause additional variability in  $H\alpha$  and  $H\beta$  measurements. Therefore, we have also checked the possibility of flaring in our sample. The short exposure spectral time series of the data in this study also allows us to quantify the possibility of flares during our observations. For this purpose, we have utilized the method proposed by [Hilton et al. \(2010\)](#) by determining the “flaring line index” (FLI). FLI for the  $H\alpha$  and  $H\beta$  lines are defined as ([Hilton et al.](#)

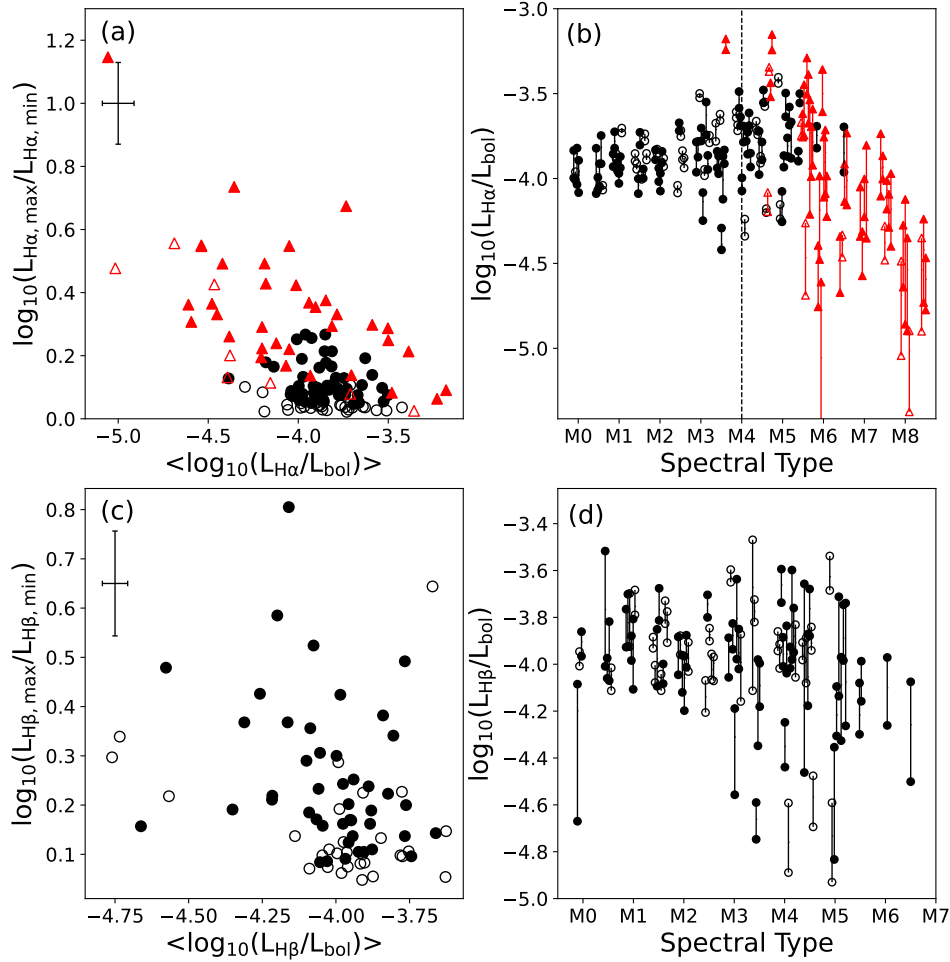


**Figure 7.** The distribution of derived activity strengths ( $L_{H\alpha}/L_{bol}$  and  $L_{H\beta}/L_{bol}$ ) for  $H\alpha$  and  $H\beta$  (top-right panel for  $H\alpha$  and bottom-right panel for  $H\beta$ ). The solid lines connect the maximum and minimum activity strength values measured for each source. The positions of objects are displaced horizontally for clarity. The vertical solid dashed line in panel (b) shows the break occur at M4, after this the activity starts to decline. Top-left and bottom-left panels show the variation of the ratio of maximum to minimum values with respect to the mean values of the activity strength  $H\alpha$  and  $H\beta$ , respectively. Symbols have the same meaning as in Fig. 3.

2010),

$$FLI = \bar{l}/\sigma \quad (5)$$

where  $\bar{l}$  is the mean value of the continuum subtracted flux in the line region, and  $\sigma$  is the standard deviation of the continuum. FLIs are useful where emission-line strengths are weak and/or continuums are noisy. The statistics of FLIs of a given spectral time series would then be used to decide if a flare occurred in the observing window, based on the following criteria by [Hilton et al. \(2010\)](#):

- (1) For strong emission line sources (i.e, mean FLI values for both  $H\alpha$  and  $H\beta$  emission of a time series are  $> 3$ ), if the maximum(FLI) and minimum(FLI) are differed by more than 30%, they are characterized as a flaring source during the time series observations.
- (2) For weak emission line sources (i.e, mean FLI values for both  $H\alpha$  and  $H\beta$  emission of a time series are  $< 3$ ), if the maximum(FLI) - minimum(FLI)  $> 3$ , they were classified as flaring sources.
- (3) For those sources which could not be categorized as

strong/weak emission line sources (i.e, mean FLI value  $> 3$  for  $H\alpha$  but  $< 3$  for  $H\beta$ ), if both the above two conditions were satisfied, they were classified as flaring sources.

Thus, after applying the above criteria, we found that out of 75 objects that showed both the  $H\alpha$  and  $H\beta$  emissions, 53 objects were found to be in a flaring state at the time of observations. Out of these 53 objects, 38 were earlier classified as variable sources based on the  $\chi^2$  minimization method as discussed in Section 3.2.

Thus, it appears that the flaring events could be a major cause of short-term variability seen in the EW light curves. Table 3 shows the flaring status of all 75 objects along with their mean FLI values for  $H\alpha$  and  $H\beta$ . [Hilton et al. \(2010\)](#) noticed that the short-term variability in chromospheric emission could be due to low-level flaring events. In a recent study by [Medina et al. \(2022\)](#), the author suggested that the flares are the most suitable mechanism to describe  $H\alpha$  variability on active mid-to-late M dwarfs. They have also mentioned that this scenario is not suitable for inactive early M dwarfs, where this chromospheric emission



variability comes from the roughly constant emission from star spots or plages rotating into and out of view on inactive early M-dwarfs. However, there are very few studies that tried to explore the short-term variations and hence, a better time resolution could very well be a key to establishing such a hypothesis.

#### 4 RESULTS FROM PHOTOMETRY: ROTATION PERIOD AND STAR-SPOT FILLING FACTOR

In the last decade, TESS and Kepler/K2 missions (Caldwell et al. 2010; Koch et al. 2010; Howell et al. 2014; Ricker et al. 2015) have provided unprecedented cadence and photometric precision for a variety of stellar sources. Such high cadence data is complementary to our spectroscopy analysis. Thus, we have utilized these photometric light curves to determine the rotation periods of the objects in our sample. While for this study, we wished to explore the period dependence of various activity proxies ( $H\alpha$  EW,  $L_{H\alpha}/L_{bol}$ , etc.). Some of these findings are discussed below.

70 of the 83 M dwarfs in our sample were observed by TESS in 2014-2021 in various sectors. Data reduction pipelines from the Science Processing Operations Center (SPOC: Jenkins et al. (2016)) and the Quick Look Pipeline (QLP: Huang et al. (2020)) are used to derive the light curves of these sources, where the Simple Aperture Photometry (SAP) flux is used. For most sources, data with 2 minutes cadence are available and used in this study. In some cases, where this high cadence data were not available, 30 minutes cadence data were used. Of the remaining 13 sources, where TESS light curves were not available, we could find the photometric light curves of 5 of the sources, with 30 minutes cadence, in the Kepler/K2 data archive. The details are given in Table 3. TESS and Kepler/K2 light curves are also used to determine the rotation periods of the objects from the Lee et al. (2010). Light curves of 31 (of total 43) objects were found in these archives. The details are given in Table 4.

##### 4.1 Rotation Period

The rotation periods ( $P_{rot}$ ) are measured by quantifying the periodic brightness variations in the light curve, which are caused by the starspots on the surface of the objects. These rotation periods have been determined by the Generalized Lomb-Scargle periodogram as discussed in Zechmeister & Kürster (2009). The period of the maximum power was further cross-checked with the phase folded light curves by visual inspection. Out of 106 sources where the light curves were available, the rotation periods of 82 objects were determined with the above method.

The rotation periods of all the objects are listed in Table 3 and Table 4, respectively. They are found to be in the range of  $\sim 0.2$ -10 days. These periods are plotted against the spectral type in Fig. 8. The derived periods conformed to the general trend seen in the other studies (West et al. 2015; Newton et al. 2017; Jeffers et al. 2018), wherein the rotation periods were found to be shorter for later spectral types. The distribution of the variability indicators, namely,  $\Delta EW$ ,  $RMS(EW)/\langle EW \rangle$ , and  $Max(EW)/Min(EW)$  as well as ac-

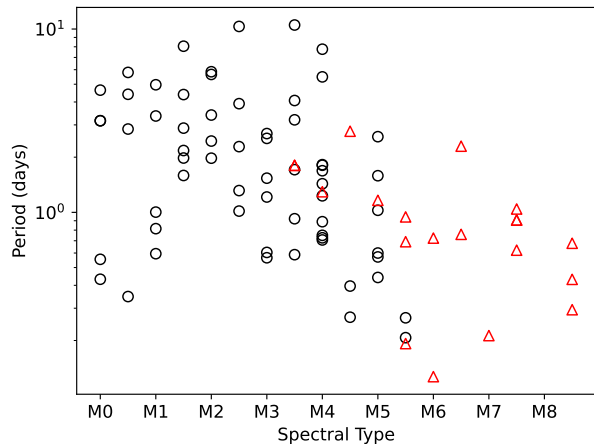


**Figure 8.** Distribution of the derived rotation periods of M dwarfs with the spectral type. Sources of this study and from Lee et al. (2010) are shown in black circles and in red triangles, respectively.

tivity strengths ( $L_{H\alpha}/L_{bol}$  and  $L_{H\beta}/L_{bol}$ ) (see Sections 3.2 and 3.3) with respect to rotation periods are shown in Fig. 9.

Various magnetic activity indicators have been used in the past to explore the relationship between the magnetic field strength and stellar rotation (Douglas et al. 2014; West et al. 2008, 2015; Newton et al. 2017; Jeffers et al. 2018). Similar to West et al. (2015), Jeffers et al. (2018), and Duvvuri et al. (2022), we also find that M dwarfs with longer periods show less variability. Duvvuri et al. (2022) suggested that these trends may be a function of the total surface area of active regions, the depth of the chromosphere subject to variable energy deposition via microflares or Alfvén waves, magnetic field topology, etc. It has also been known that in M dwarfs, there is a clear decrease in the strength of activity with increasing rotation period (West et al. 2015; Jeffers et al. 2018). However, an interesting behaviour can be noticed in the panels *a*, *b*, *c* (for  $H\alpha$ ) and *e*, *f*, *g* (for  $H\beta$ ), when we consider the spectral types as well. Here the short-term variability indicators display a very clear increase for the faster rotating M dwarfs with a rotation period  $< 2$  days, and most of these objects belong to the later types (M4-M8) as seen in Fig. 8. Here we intend to show the variation of the rotation period as a function of the spectral type we have derived for our sample. Our analysis is consistent with the trends seen in other studies such as Jeffers et al. (2018). Thus such high variability in late-type fast rotators M dwarfs reflects an overall shift in their magnetic field, leading to less uniform spatial and temporal dissipation as suggested by Kruse et al. (2010).

Another important parameter is the Rossby number ( $R_0$ ), which is the ratio of the rotation period to the convective overturn timescale. It is used to compare activity strengths across mass and rotation period ranges. We have used the empirical calibration from Wright et al. (2011) (Eq. 10, page-11) to determine convective overturn timescales. Our samples show a saturated relationship between activity strengths and  $R_0$  (see Fig. 12). Since the Rossby number for our samples ranges from 0.0003-0.2, the observed saturation is expected. A power-law decay in

**Table 2.** The derived variability parameters for H $\alpha$  and H $\beta$  emission lines for the sources of this study, along with the activity strengths ( $\log_{10}(L_{H\alpha}/L_{bol})$  and  $\log_{10}(L_{H\beta}/L_{bol})$ ). The  $p$ -values are determined from the  $\chi^2$  minimisation of EW light curves. See Section 3.2 for details. The sources which are characterized as variable are marked with (\*). The full table for all the sources is given in Table-2 of Appendix-III in the supplementary material.

Source ID	Source name	emission line	Median H $\alpha$ EW H $\beta$ EW	Minimum H $\alpha$ EW H $\beta$ EW	Maximum H $\alpha$ EW H $\beta$ EW	$\Delta$ H $\alpha$ EW H $\beta$ EW	RMS H $\alpha$ EW H $\beta$ EW	Mean $\log_{10}(L_{H\alpha}/L_{bol})$ $\log_{10}(L_{H\beta}/L_{bol})$	P-value H $\alpha$ H $\beta$
1	PM J03332+4615S*	H $\alpha$	-2.333 $\pm$ 0.065	-1.717 $\pm$ 0.062	-2.492 $\pm$ 0.061	0.775 $\pm$ 0.087	0.232 $\pm$ 0.022	-3.883	0.0000
		H $\beta$	-1.372 $\pm$ 0.085	-0.413 $\pm$ 0.091	-1.590 $\pm$ 0.086	1.177 $\pm$ 0.125	0.349 $\pm$ 0.031	-4.199	0.0000
2	PM J03416+5513	H $\alpha$	-1.688 $\pm$ 0.047	-1.587 $\pm$ 0.045	-1.775 $\pm$ 0.052	0.188 $\pm$ 0.068	0.051 $\pm$ 0.012	-3.984	0.2298
		H $\beta$	-1.818 $\pm$ 0.085	-1.690 $\pm$ 0.076	-1.947 $\pm$ 0.087	0.258 $\pm$ 0.116	0.080 $\pm$ 0.020	-3.981	0.4134
--	--	--	--	--	--	--	--	--	--

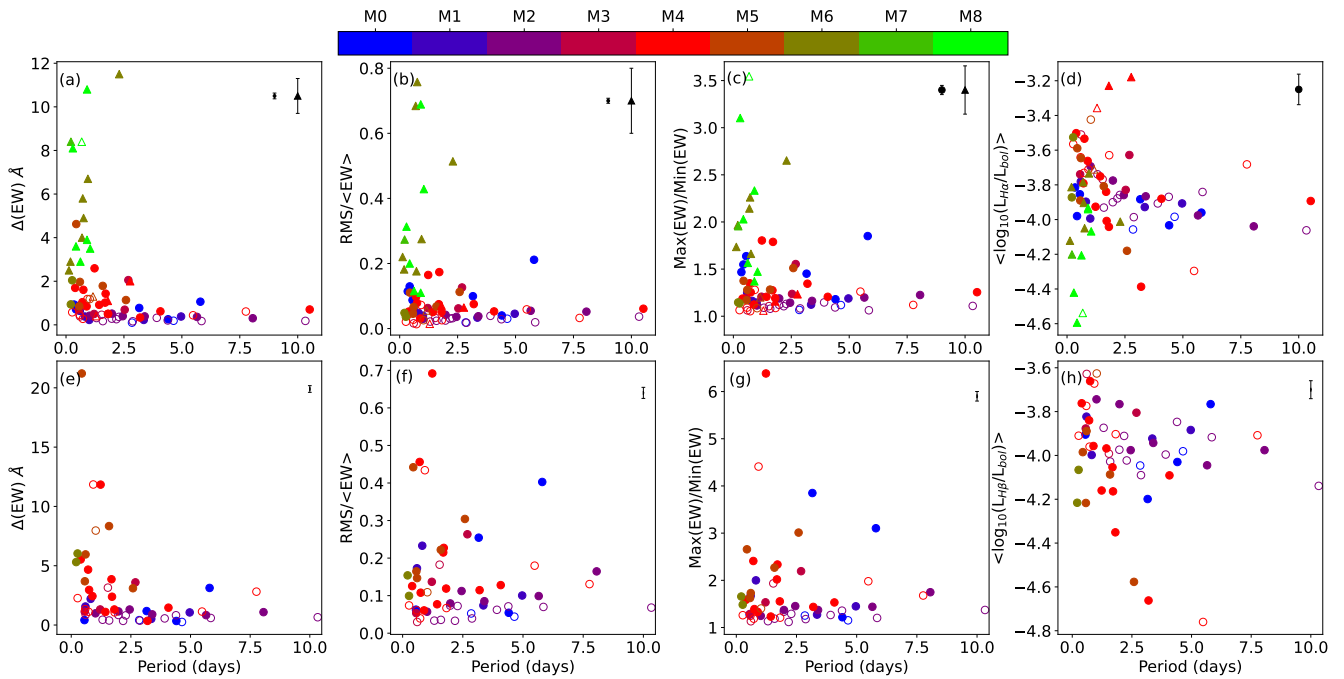


**Figure 9.** Figure shows the distribution of  $\Delta(EW)$ ,  $RMS(EW)/\langle EW \rangle$ ,  $R(EW) = \text{Max}(EW)/\text{Min}(EW)$  and mean activity strengths with their rotational periods. Top panels are for H $\alpha$  and bottom panels are for H $\beta$  emission. The median errorbars of the data points are shown on the top-right corner. Symbols have the same meaning as in Fig. 3

$L_{H\alpha}/L_{bol}$  with increasing  $R_0$  ( $>0.2$ ) could not be seen, which breaks near  $R_0 \sim 0.2$ .

There are some studies (Radick et al. 1998; Hall et al. 2009; Buccino et al. 2011; Fuhrmeister et al. 2019; Schöfer et al. 2022; Medina et al. 2022; Duvvuri et al. 2022), which estimate the rotation period using chromospheric activity indicators (H $\alpha$ , Ca II IRT, etc.) or using photospheric activity indicators (TiO 7050 absorption band, etc.). Fuhrmeister et al. (2019) emphasized that H $\alpha$  and the Ca II IRT lines are well suited for period searches only if the star is dominated by a periodic pattern of H $\alpha$  or Ca II plages and not dominated by micro-flaring and another intrinsic variability. These studies suggest that young, active stars become fainter as their chromospheric emission (e.g., H $\alpha$ ) increases, whereas older, less active stars become brighter as their chromospheric emission increases. These studies also interpreted the cause of this behavior as the long-term variability of young stars is spot dominated, whereas, for older stars, it is faculae dominated. Therefore, it is instructive to explore such behavior in spite of having a relatively shorter time series. The typical rotation period of the stars in our sample is in the range of 0.2-10 days, while our spectral time

series for a single source is around 0.7-2.3 hours. Thus, the observed fraction of the rotation period of the stars in our sample is very small, ranging from 0.4 to 24% of the period. We have, nevertheless, tried to map the derived EWs of H $\alpha$  with respect to the stellar rotation phase.

To determine the phase of the object during the observations of the spectral time series, we have extrapolated the photometric light curve to our observing window by fitting a sinusoidal function, assuming the photometric light curve modulation does not vary significantly. We could do this for 49 of the sources. The analyses for two of the sources are shown in Fig. 10 and Fig. 11. While the plots for all the sources are given in Appendix-II in the supplementary material. We do notice that five sources show (visually) an ‘apparent’ correlation of H $\alpha$  EW with the phase of the photometric light curve (i.e., H $\alpha$  EW increases with increases in the photometric brightness), and another nine sources show an ‘apparent’ anti-correlation. However, such ‘apparent’ relations are noticed only visually, and therefore we do not attempt to draw any conclusion here. A longer time series will indeed be very useful to say anything conclusively regarding the presence of such plausible correlations. We shall attempt

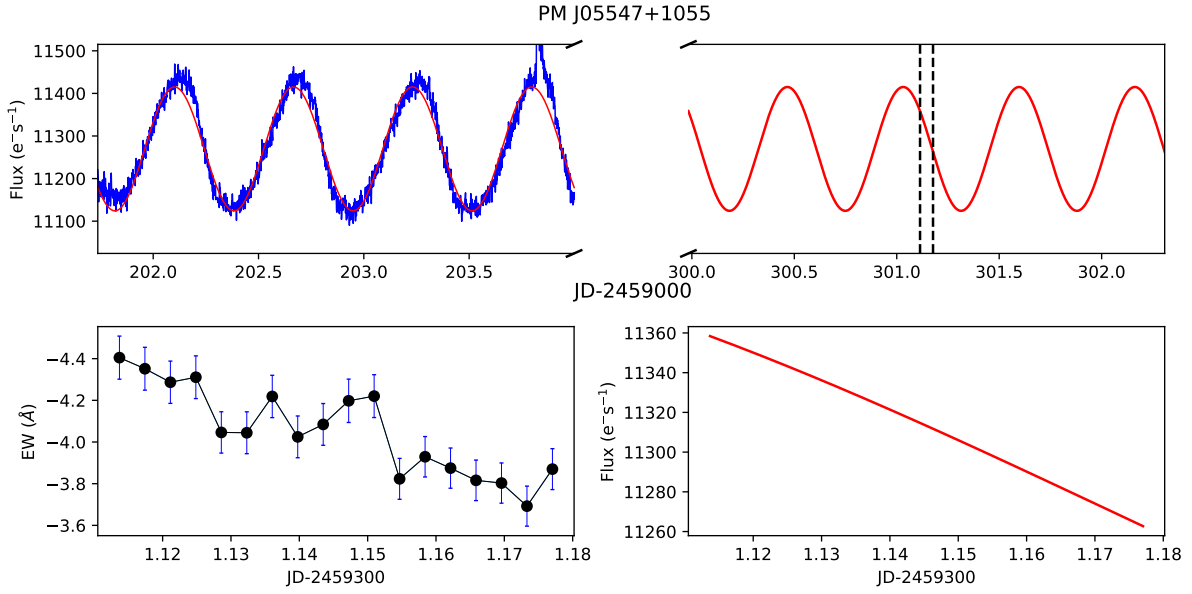


**Figure 10.** The top panel shows the extrapolated sinusoidal fit (red) with the photometric light curve (blue). The vertical line shows the start and end of our monitoring spectroscopic observations. The bottom left and right panels show the H $\alpha$  equivalent width light curve and corresponding extrapolated photometric light curve, respectively, showing a correlation between the star’s brightness and H $\alpha$  EW.

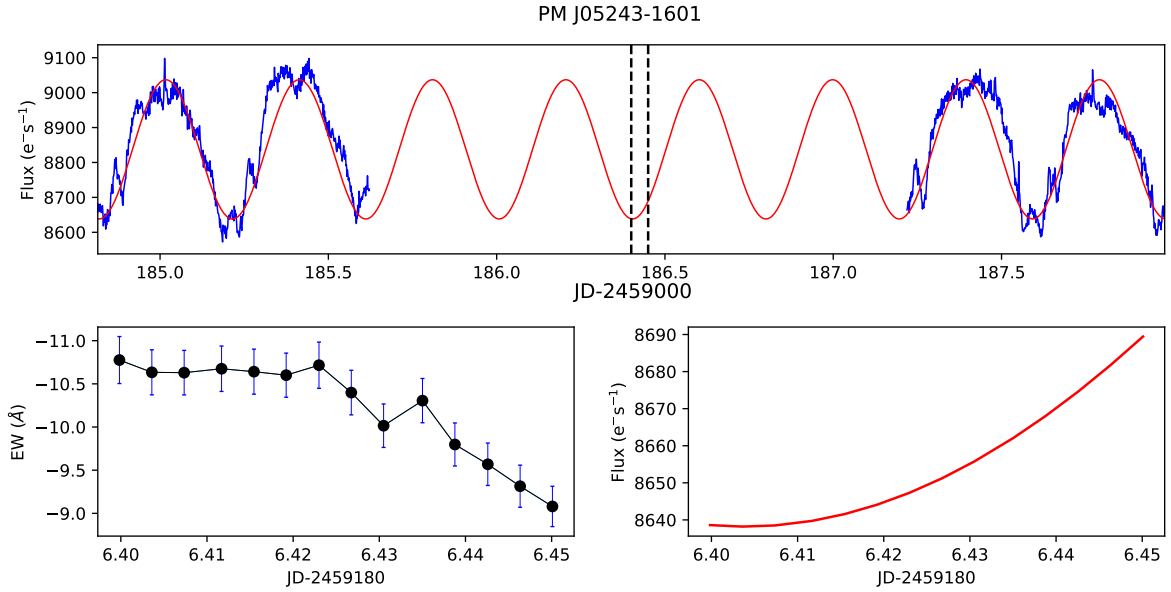


**Figure 11.** The figure description is the same as Fig. 10 but shows an anti-correlation between the star’s brightness and H $\alpha$  EW.

to further obtain a longer time series for these sources for such purposes.

#### 4.2 Filling Factor

The light curves from TESS and Kepler/K2 are also used to determine the star-spot filling factors. We have computed these values for the objects in this study as well as from Lee et al. (2010). The star-spots on the photosphere are the regions where the magnetic flux is much stronger, and most of the stellar flares occur. The star-spot filling factor gives the fractional area covered by star-spots ( $A_{spot}/A_{star}$ ).

The filling factors are computed by the following relations (Jackson & Jeffries 2013; Maehara et al. 2017; Guenther et al. 2021) :

$$\frac{A_{spot}}{A_{star}} = \left( \frac{\Delta F}{F} \right)_{spot} \left[ 1 - \left( \frac{T_{spot}}{T_*} \right)^4 \right]^{-1} \quad (6)$$

where  $A_{star}$  is the area of the stellar disk,  $A_{spot}$  is the area of the spots on the stellar disk, and  $T_*$  and  $T_{spot}$  are the temperature of the star and the star-spot respectively.  $\Delta F/F_{spot}$  is the brightness variation amplitude of the rotation modu-

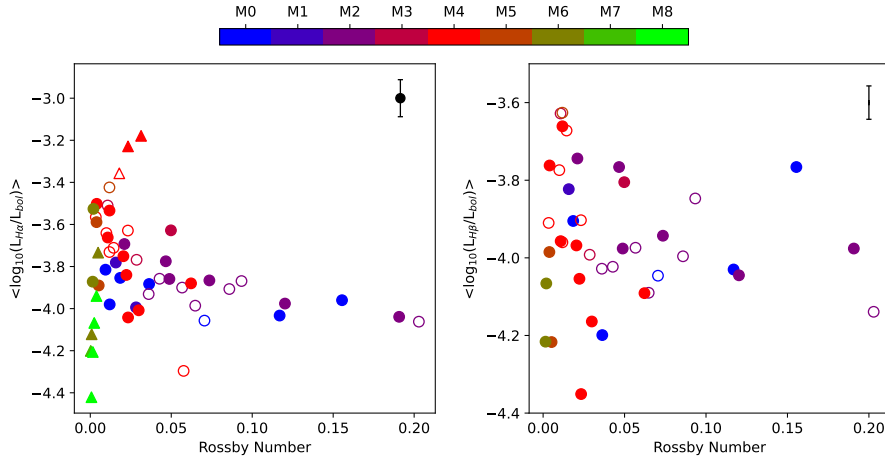


**Figure 12.** The distribution of derived activity strengths  $L_{H\alpha}/L_{bol}$  (left panel) and  $L_{H\beta}/L_{bol}$  (right panel) with respect to Rossby number. The median errorbars of the data points are shown on the top-right corner. Symbols have the same meaning as in Fig. 3.

**Table 3.** Derived rotation periods and star-spot filling factors of the objects of this study using TESS and Kepler/K2 light curves. The rotation periods from the literature survey are also mentioned with references and remark (if any). The observing details from TESS and Kepler/K2 archives and computed mean values of FLI for  $H\alpha$  and  $H\beta$  emissions from the spectral time series are also mentioned. The flaring sources (as per FLI criteria) during the spectroscopy observations are marked with (\*) in the source-name column. See Section 4 for discussion. In the third column (mission/year/author), the notation ‘T’ represents TESS sector and a ‘K’ represents K2 campaign. The full table for all the sources is given in Table-3 of Appendix-III in the supplementary material.

Source ID	Source name	Mission/Year/ Author	Exposure time (s)	Rotation period (days)	Rotation Period from literature <sup>b</sup> (days)	Ref.	$T_{spot}$ (K)	Filling factor %	Mean FLI $H\alpha$	Mean FLI $H\beta$
1	PM J03332+4615S*	T-18/2019/QLP	1800	3.160	-	-	3192	36	$10.40 \pm 1.72$	$2.65 \pm 0.95$
2	PM J03416+5513*	T-19/2019/SPOC	120	4.641	8 <sup>1</sup>	4	3145	6.2	$6.97 \pm 0.62$	$4.50 \pm 0.45$
3	PM J07151+1555*	T-33/2020/SPOC	120	0.554	0.555	6	3239	9.6	$12.05 \pm 1.83$	$4.67 \pm 0.42$
--	--	--	--	--	--	--	--	--	--	--

a: References- 1. Messina et al. (2017), 2. Houdebine et al. (2016), 3. Vidotto et al. (2014), 4. Magaudda et al. (2020), 5. Newton et al. (2017), 6. Kiraga (2012), 7. Schöfer et al. (2019), 8. Stelzer et al. (2022), 9. Rodríguez Martínez et al. (2020), 10. Raetz et al. (2020), 11. Newton et al. (2016), 12. Günther et al. (2020), 13. Newton et al. (2018), 14. Houdebine et al. (2017).

b: Sources having different rotation periods from this study, computed with the following method: 1. This was estimated by the empirical relation between Chromospheric activity and rotation period, 2. This was estimated by using All Sky Automated Survey (ASAS) photometry data (having low cadence; mostly one data point per day), 3. This was estimated by Hungarian-made Automated Telescope Network (HATNet) survey photometry data (they studied 1568 stars), 4. This was estimated with the help of  $v\text{-sin}i$  and the radius of the star, where the star’s radius was calculated using empirical relation, 5. Messina et al. (2016) estimated this rotation period using their own photometry observation of this previously known visual binary stars, 6. This was estimated by using photometry data from MEarth (having cadence of 30 minutes; they studied 387 stars).

**Table 4.** The derived rotation periods and star-spot filling factors for 31 sources of Lee et al. (2010). The  $T_{eff}$  values for these sources are estimated from  $T_{eff}$  versus spectral type relation given in Rajpurohit et al. (2013). See Section 4 for discussion. The full table for all the sources is given in Table-4 of Appendix-III in the supplementary material.

Source name	Mission/Year/ Author	Exposure time (s)	Rotation period (days)	Rotation Period from literature (days)	Ref.	$T_{eff}$ (K)	$T_{spot}$ (K)	Filling factor %
G99-049	T-33/2020/SPOC	120	1.805	1.809	5	3100	2792	1.2
LHS1723	T-32/2020/SPOC	20	-	88.5	5	3100	2792	0.5
L449-1	T-32/2020/SPOC	120	1.296	-	-	3100	2792	2
--	--	--	--	--	--	--	--	--

lation caused by the star-spots. The temperature difference between the photosphere and starspots is a function of the photospheric temperature of the stars (Berdyugina 2005). Thus,  $T_{spot}$  can be estimated with the following relation (Berdyugina 2005; Maehara et al. 2017; Notsu et al. 2019; Guenther et al. 2021):

$$T_{spot} = T_* - 3.58 \times 10^{-5} T_*^2 - 0.249 \times T_* + 808 [K] \quad (7)$$

For the sources in this study, we have used  $T_{eff}$  as determined in Section 3 whereas for the sources of Lee et al. (2010)  $T_{eff}$  are determined using the spectral type -  $T_{eff}$  relation of Rajpurohit et al. (2013) (see Fig.5 therein).

The derived filling factors are given in Table 3. We note that these filling factors are the lower limits as many active stars could have polar spots (Guenther et al. 2021). For our samples, the spot temperatures and filling factors are mostly found between  $\sim 2700\text{-}3200$  K and  $\sim 0.5\text{-}20.0\%$ , respectively.

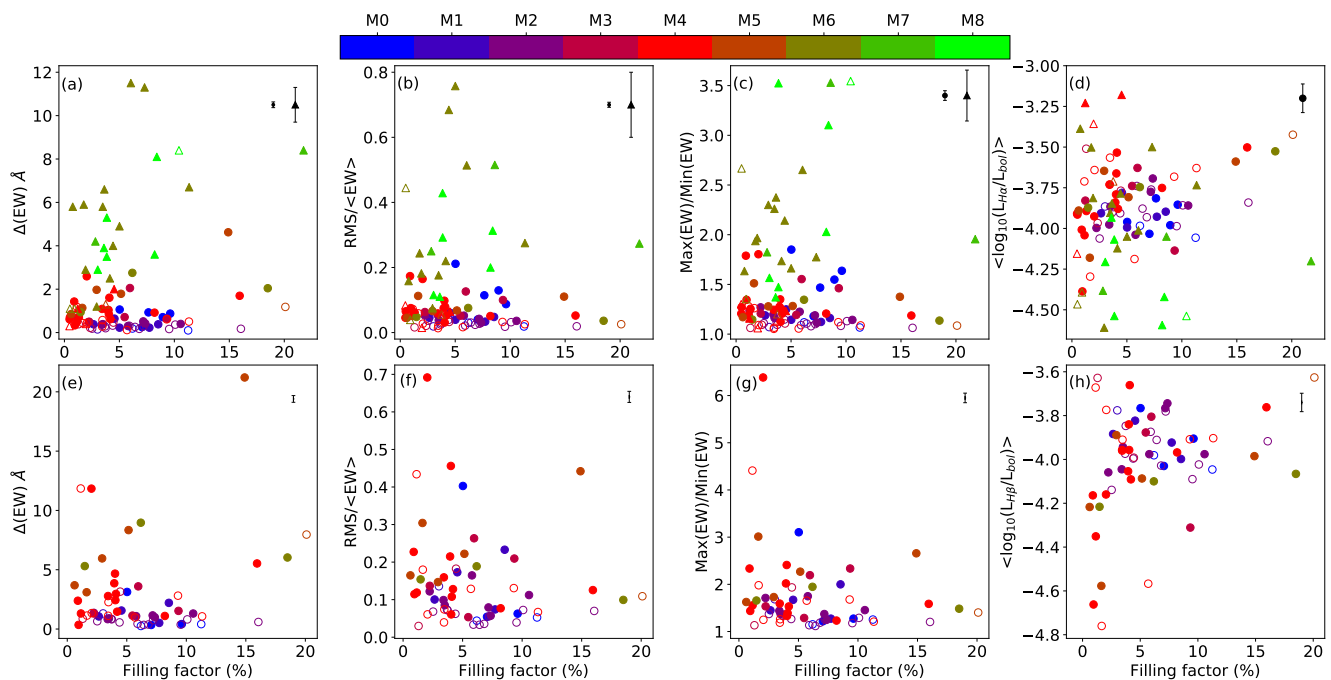


**Figure 13.** Distribution of variability indicators (same as Fig. 9) but with respect to star-spot filling factors.

While for the sources of Lee et al. (2010), these values are mostly found to be in the range of  $\sim 2460$ - $2800$  K and  $\sim 0.5$ - $21.8\%$ , respectively.

We have also explored the variations in H $\alpha$  and H $\beta$  variability indicators with respect to the derived filling factors. Fig. 13 show these plots similar to Fig. 9 (for rotations). It is postulated (Bell et al. 2012) that stars having large filling factors would have high activity strength and lesser variability and vice versa. This trend is noticeable in panels (b) and (f) for H $\alpha$  and H $\beta$  respectively, i.e.,  $\text{RMS}(\text{EW}) / \langle \text{EW} \rangle$  show a downward trend for higher filling factors, i.e., high activity stars (large  $\langle \text{EW} \rangle$ ) which are less variable (low  $\text{RMS}(\text{EW})$ ) tend to have high filling factors.

## 5 AGES

As stars are gravitationally bound, they orbit the centre of the Galaxy. While interacting with various giant molecular clouds and other passing stars, their orbit gets altered via kinematic kick due to their interaction with other objects, causing the stars to separate from the plane of the Galaxy as they age (Kiman et al. 2019). The ages of stars in the StarHorse project are determined using a Bayesian approach that incorporates geometric, age, and metallicity priors for the major components of the Galaxy (Queiroz et al. 2018; Anders et al. 2019). To compute these ages, a likelihood is calculated by comparing observed parameters with the PARSEC and TRIESTE Stellar Evolution Code (PARSEC; Bressan et al. 2012). In the present study, the observable quantities used include surface temperature and gravity values derived within this paper, as well as magnitudes obtained from the 2MASS survey (Cutri et al. 2003) and parallaxes and magnitudes from Gaia Data Release 3 (Gaia Collaboration et al. 2022). However, it is important

to note that the ages estimated by StarHorse for this particular sample may exhibit significant uncertainties due to the absence of metallicity measurements and the increased complexity of isochrone fitting outside the subgiant range (see Queiroz et al. (2023) for further details). Table 5 gives the details of the parameters used to estimate the age with derived ages.

The H $\alpha$  luminosity ( $L_{\text{H}\alpha}/L_{\text{bol}}$ ) can be used as the age indicator since the young stars tend to have higher magnetic activity, whereas the old stars are less active or inactive (West et al. 2008; Newton et al. 2017). However, these relationships are not sustained because we currently do not have the data to substantiate them. Although it could be the case that fully convective stars do not follow this particular relationship. The possibilities for any such relations, in the case of M dwarfs, have been investigated in various recent studies (Riedel et al. 2017; West et al. 2008; Newton et al. 2017; Kiman et al. 2021).

In Fig. 14, we have shown the derived age of stars in our sample against the similar data provided by Kiman et al. (2021) where the activity strength ( $L_{\text{H}\alpha}/L_{\text{bol}}$ ) is attempted to be correlated with the age of the stars. To compare our values with them, we have also divided our samples into spectral type bins (M0-M2, M3-M6, and M7-M9). The age-activity strength values for data of our study seem to be matched with the relation given by Kiman et al. (2021) for early to mid-type of M dwarfs, though they differ from the relation provided by West et al. (2009). This difference has also been noted by Kiman et al. (2021) for their data set, who remarks that it is likely that West et al. (2009) has overestimated the activity strength of their sample. We also noticed that the age of early M dwarfs (M0-M2) in our samples, exceeding the age cutoff given in West et al. (2009), though it follows the empirical relation given by Kiman et al. (2021).

Further, the observed H $\alpha$  variability in our sample is

**Table 5.** Details presented in this table are used to determine the age (last column) of our sources. The coordinates RA, DEC and J,H,K magnitudes are taken from SIMBAD and all other parameters taken from Gaia Data Release 3 (Gaia Collaboration et al. 2022). The full table for all the sources is given in Table-5 (our sources) and Table-6 (Lee et al. (2010) sources) of Appendix-III in the supplementary material.

Source ID	RA (hh:mm:ss)	DEC (dd:mm:ss)	J	H	K	$g$	$bp$	$rp$	Proper motion in RA (mas year <sup>-1</sup> )	Proper motion in DEC (mas year <sup>-1</sup> )	Radial velocity (km s <sup>-1</sup> )	Parallax (mas)	Age (Gyr)
1	03 33 14.04	+46 15 18.97	8.382	7.770	7.592	10.497	11.305	9.590	68.9023 ± 0.0146	-172.5847 ± 0.0146	-14.2682 ± 8.3249	27.4809 ± 0.0158	3.250 ± 1.475
2	03 41 37.27	+55 13 06.83	8.347	7.649	7.499	10.557	11.469	9.607	96.7821 ± 0.0149	-116.6387 ± 0.0155	-4.6260 ± 0.3481	27.9199 ± 0.0145	6.970 ± 4.216
3	07 15 08.78	+15 55 44.95	8.741	8.144	7.973	10.972	11.686	10.007	209.7643 ± 0.0247	-169.0688 ± 0.0206	21.2126 ± 29.2719	18.9026 ± 0.0207	-
--	--	--	--	--	--	--	--	--	--	--	--	--	--

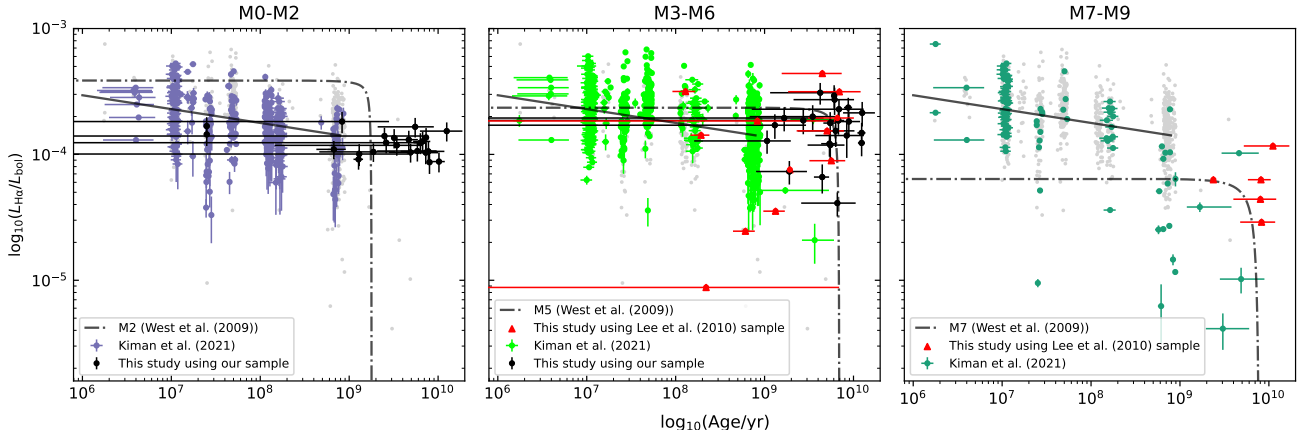


**Figure 14.** The figure shows the derived values of activity strength ( $L_{H\alpha}/L_{bol}$ ) and age for the source in this study (black circles and red triangles) against similar data provided by Kiman et al. (2021) (see figure-10 of their article). The empirical relations provided by West et al. (2009) (dot-dashed line) and Kiman et al. (2021) (solid line) are also plotted. These plots are reproduced from the data presented in Kiman et al. (2021) by utilising the plotting script provided by them. The background grey data points in each panel represent the complete sample of Kiman et al. (2021).

shown with respect to the derived ages and spectral type in Fig. 15, and higher short-term variability is noticed in older late-type stars. We notice that Kiman et al. (2021) has also tried to relate the  $H\alpha$  variability with the age of the stars (figure-7 of their article), where higher  $H\alpha$  variability is seen for younger objects. However, their sample covers a larger age span ( $6.5 < \log(\text{age}/\text{years}) < 9$ ). Moreover, the  $H\alpha$  variability in their sample is not derived from any systematic short-term time series (such as ours) and therefore, it may not be prudent to compare these results.

## 6 DISCUSSION

In this work, we have studied the short-term activity of M dwarfs through  $H\alpha$  variability as a proxy. Though our sources belong to M0-M6.5 spectral classes, a similar study by Lee et al. (2010) provided a complementary set of 43 M dwarfs in mostly M3.5-M8.5 spectral types. Thus this set of 126 sources spanning a full range of M0-M8.5 is suitable for exploring the distribution of derived variability across the spectral types. The availability of photometric data from the TESS and Kepler/K2 missions also proved extremely useful for relating the derived short-term spectroscopy variability with their rotation periods and age.

We present the results of our analysis as follows:

(i) In our data set of 126 sources, the activity strengths are determined to be close to  $\sim 10^{-3.8}$  for the spectral types M0-M4 and then decrease to  $\sim 10^{-5.0}$  for mid to late-type

M dwarfs. The derived mean activity strengths ( $\langle L_{H\alpha}/L_{bol} \rangle$  and  $\langle L_{H\beta}/L_{bol} \rangle$ ) over this short-term time series are consistent with the trend seen in Bell et al. (2012); Lee et al. (2010), where the activity strengths decrease for the later spectral types, and the corresponding variability was found to be higher.

(ii) We studied the variability in  $H\alpha$  and  $H\beta$  using various variability indicators. A noticeable difference in these indicators is seen between early-type (M0-M3) and late-type ( $> M3$ ) M dwarfs, which is partially due to the intrinsic variability of  $H\alpha$  (Kruse et al. 2010; Bell et al. 2012). These breaks in the activity strength at spectral type M3, could be explained due to a change in the magnetic dynamo mechanism at the fully convective boundary.

(iii) Using the cumulative normalized-structure function, we investigated the timescales of variability in  $H\alpha$  EW time series. The observed  $H\alpha$  variability time scale for early M dwarfs (M0-M2) is found to be  $\sim 40 - 60$  minutes, whereas, for mid-type M dwarfs (M3-M5), it is found to be longer than 60 minutes. This trend is also seen by (Kruse et al. 2010), but we noticed that their observed spectra are not in good cadence. We speculate that different  $H\alpha$  variability time scales could be related to the varying strength of magnetic activity as a function of spectral type.

(iv) Using the high cadence photometric data from TESS and Kepler/K2 missions, we derived the rotation period of 82 M dwarfs in our sample, which ranges between  $\sim 0.2-10$  days. We find that late-type M dwarfs (M6-M8.5) with a rotation period of  $< \sim 2$  days show higher variability. This behaviour could be caused by the faster-rotating stars as

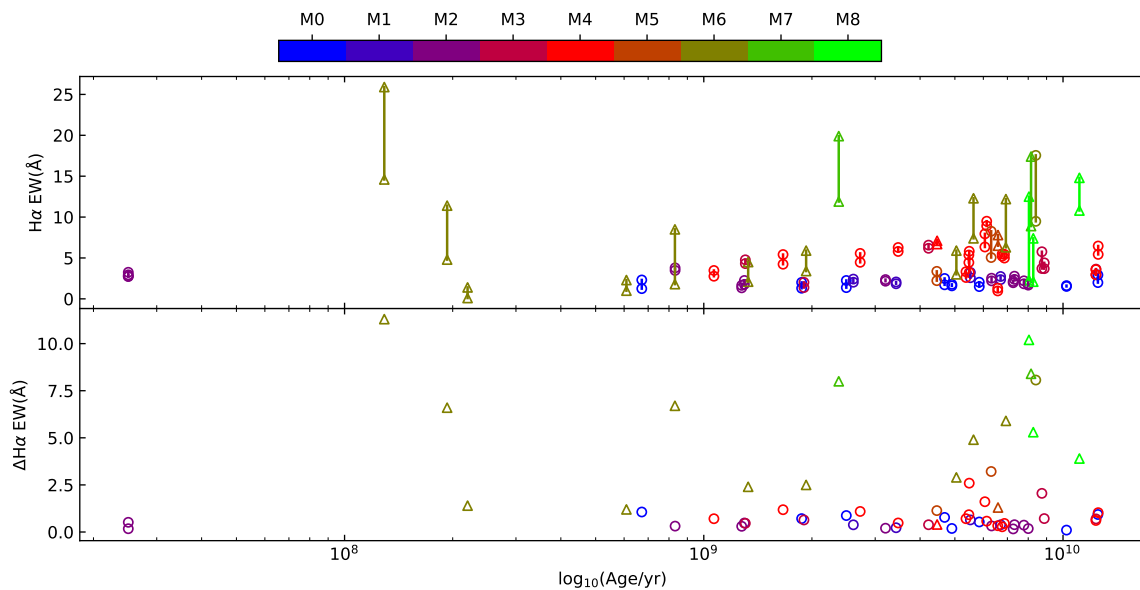


**Figure 15.** The figure shows H $\alpha$  variability in our sample (open circle) and Lee et al. (2010) sample (open triangle) as a function of age. The top panel shows the H $\alpha$  EWs for the sources. The maximum and minimum of the H $\alpha$  EWs in the time series for a star are connected with a line. The bottom panel shows  $\Delta$  EW in the time series.

they are seen to demonstrate magnetic activity in shorter time scales, and it is believed that active dynamo is responsible for this phenomenon (Wright et al. 2011). While the observed variabilities in H-alpha can be the base variabilities due to the appearance and disappearance of starspots or pledges on them (Medina et al. 2022), it is their fast-rotating nature that leads us to believe that we are capturing part of their active phases when they are flaring more and showing the variability in H-alpha. It is also to be mentioned that surface manifestation of higher magnetic activity (such as starspots) will lead to more flares. However, to establish our conjecture, we will require long-time systematic observations of the same objects.

(v) To determine the rotation-activity relation, we have calculated the Rossby number ( $R_0$ ). We find that ( $L_{H\alpha}/L_{bol}$ ) maintains the saturated value till  $R_0 < 0.2$ . With rotation above a certain threshold, as suggested by Newton et al. (2017) and Wright et al. (2018), magnetic activity maintains a constant value, while at slower spins, magnetic activity and rotation are correlated.

(vi) Though the total duration of our spectral time series is only a small fraction of the rotation period (0.4-24%), for most of the sources, we attempted to check if any correlation could be observed between H $\alpha$  EW and the rotation phase. We notice apparent correlation/anti-correlation in some of the sources, which in some studies (Baliunas 1988; Buccino et al. 2011; Fuhrmeister et al. 2019; Medina et al. 2022) is interpreted as the presence of spots/bright faculae. However, considering the smaller covering fraction of the phase, we restrict ourselves from interpreting this result.

(vii) Using kinematics and parallaxes from GAIA DR3, we could estimate the age of 63 M dwarfs. Though the ages of M dwarfs in our sample range from 0.025-12.528 Gyr, from our analysis, we find that older late-type M dwarfs show higher variability in H $\alpha$ .

(viii) The sources having smaller filling factors were found

to be more variable across the spectral range. However, the late-type sources are more prominent in the variability scale. A large filling factor could give rise to a strong and persistent H $\alpha$  emission as opposed to the objects having low filling factors. Any minor change (such as the appearance of new small active regions, micro-flare, etc.) on the highly active stars with high filling factors would not be as prominent as for the stars with low filling factors (lower H $\alpha$  emission). Thus, stars with smaller filling factors are expected to be more variable, as we notice in our analysis. The same inference has also been drawn by Bell et al. (2012).

Variability in M dwarfs on the shorter time scales (a few minutes) is very significant as they are postulated to originate from the small energetic events or the appearance/disappearances of starspots on the stellar surfaces (Bell et al. 2012; Medina et al. 2022). Such physical origins of the observed variability in H-alpha are inherently related to the dynamics of stellar magnetic fields, which are known to be coupled with stellar rotation. Thus, studies of variabilities at these short time scales could probe the possible link between activity and rotation. Such studies are beneficial for detecting the low-amplitude and short-duration flares, which can further explore our understanding of flare behavior and their relation with rotational phases (if any). The time scales of variability in M dwarfs are much dependent on the basic parameters (e.g., rotation, magnetic field strengths, etc.) and dynamics (such as internal dynamos) of the objects. High-activity objects with large filling factors are found to be less variable, possibly due to the requirements of more energetic events (such as large flares) to change their observational status in terms of H $\alpha$  / H $\beta$  strengths. Such energetic events may require larger time scales to build up and/or to evolve. The variability of less active stars, on the other hand, would probably be governed by the low energetic events that could occur on shorter time scales. Such stars would thus be ex-

pected to have lesser filling factors. Thus, the measurements of the time scales of the  $H\alpha$  /  $H\beta$  variations are of profound significance to understanding the underlying activity on the surface of the star. A larger sample with finer time resolution could very well be the key to unlocking the physical mechanisms responsible for such activity.

## 7 ACKNOWLEDGMENTS

The research work at the Physical Research Laboratory (PRL) is funded by the Department of Space, Government of India. VK thanks PRL for his Ph.D. research fellowship. We thank Veeresh Singh (PRL) and Rishikesh Sharma (PRL) for the useful discussions. The computations were performed on the HPC resources at PRL. J.G.F-T gratefully acknowledges the grant support provided by Proyecto Fondecyt Iniciación No. 11220340, and also from ANID Concurso de Fomento a la Vinculación Internacional para Instituciones de Investigación Regionales (Modalidad corta duración) Proyecto No. FOVI210020, and from the Joint Committee ESO-Government of Chile 2021 (ORP 023/2021), and from Becas Santander Movilidad Internacional Profesores 2022, Banco Santander Chile. This research has made use of the SIMBAD database, operated at CDS, Strasbourg, France. This paper includes data collected by the TESS and Kepler mission and acquired from the Mikulski Archive for Space Telescopes (MAST) data archive at the Space Telescope Science Institute (STScI). Funding for the TESS and KEPLER missions is provided by NASA's Science Mission Directorate. STScI is operated by the Association of Universities for Research in Astronomy, Inc., under NASA contract NAS5-26555. This research made use of Lightcurve, a Python package for Kepler and TESS data analysis.

## 8 DATA AVAILABILITY

The MFOSC-P spectroscopic monitoring data may be made available on reasonable request. The corresponding authors may be contacted for that. The TESS and KEPLER data used in this work are available on Mikulski Archive for Space Telescopes (MAST).

## REFERENCES

- Allard F., Homeier D., Freytag B., 2010, preprint, ([arXiv:1011.5405](https://arxiv.org/abs/1011.5405))
- Allard F., Homeier D., Freytag B., Schaffenberger W., Rajpurohit A. S., 2013, *Memorie della Societa Astronomica Italiana Supplementi*, **24**, 128
- Almeida L. A., Jablonski F., Martioli E., 2011, *A&A*, **525**, A84
- Anders F., et al., 2019, *A&A*, **628**, A94
- Angus R., Aigrain S., Foreman-Mackey D., McQuillan A., 2015, *MNRAS*, **450**, 1787
- Baliunas S., 1988, in Foukal P., ed., *Solar Radiative Output Variation*. p. 230
- Baroch D., et al., 2021, *A&A*, **653**, A49
- Bell K. J., Hilton E. J., Davenport J. R. A., Hawley S. L., West A. A., Rogel A. B., 2012, *PASP*, **124**, 14
- Berdugina S. V., 2005, *Living Reviews in Solar Physics*, **2**, 8
- Bochanski J. J., West A. A., Hawley S. L., Covey K. R., 2007, *AJ*, **133**, 531
- Bonfils X., et al., 2012, preprint, ([arXiv:1206.5307](https://arxiv.org/abs/1206.5307))
- Bressan A., Marigo P., Girardi L., Salasnich B., Dal Cero C., Rubele S., Nanni A., 2012, *MNRAS*, **427**, 127
- Buccino A. P., Díaz R. F., Luoni M. L., Abrevaya X. C., Mauas P. J. D., 2011, *AJ*, **141**, 34
- Caldwell D. A., et al., 2010, in Oschmann Jacobus M. J., Clampin M. C., MacEwen H. A., eds, *Society of Photo-Optical Instrumentation Engineers (SPIE) Conference Series Vol. 7731, Space Telescopes and Instrumentation 2010: Optical, Infrared, and Millimeter Wave*. p. 773117, doi:10.1117/12.856638
- Chabrier G., 2003, *ApJ*, **586**, L133
- Chabrier G., Baraffe I., 1997, *A&A*, **327**, 1039
- Chang H. Y., et al., 2017, *ApJ*, **834**, 92
- Cool A. M., Piotto G., King I. R., 1996, *ApJ*, **468**, 655
- Cutri R. M., et al., 2003, *VizieR Online Data Catalog*, p. II/246
- Dittmann J. A., Irwin J. M., Charbonneau D., Newton E. R., 2016, *ApJ*, **818**, 153
- Douglas S. T., et al., 2014, *ApJ*, **795**, 161
- Doyle L., Ramsay G., Doyle J. G., Wu K., Scullion E., 2018, *MNRAS*, **480**, 2153
- Doyle L., Ramsay G., Doyle J. G., Wu K., 2019, *MNRAS*, **489**, 437
- Dressing C. D., Charbonneau D., 2015, *ApJ*, **807**, 45
- Duvvuri G. M., Pineda J. S., Berta-Thompson Z. K., France K., Youngblood A., 2022, *The Astronomical Journal*, 165, 12
- Fuhrmeister B., et al., 2019, *A&A*, **623**, A24
- Gaia Collaboration et al., 2022, *arXiv e-prints*, p. [arXiv:2208.00211](https://arxiv.org/abs/2208.00211)
- Gillon M., et al., 2017, preprint, ([arXiv:1703.01424](https://arxiv.org/abs/1703.01424))
- Gizis J. E., Reid I. N., Hawley S. L., 2002, *AJ*, **123**, 3356
- Green P. J., Margon B., 1994, *ApJ*, **423**, 723
- Guenther E. W., Wöckel D., Chaturvedi P., Kumar V., Srivastava M. K., Muheki P., 2021, *MNRAS*, **507**, 2103
- Günther M. N., et al., 2020, *AJ*, **159**, 60
- Hall J. C., Henry G. W., Lockwood G. W., Skiff B. A., Saar S. H., 2009, *AJ*, **138**, 312
- Hawley S. L., Gizis J. E., Reid I. N., 1996, *AJ*, **112**, 2799
- Hawley S. L., Davenport J. R. A., Kowalski A. F., Wisniewski J. P., Hebb L., Deitrick R., Hilton E. J., 2014, *ApJ*, **797**, 121
- Henry T. J., Ianna P. A., Kirkpatrick J. D., Jahreiss H., 1997, *AJ*, **114**, 388
- Hilton E. J., West A. A., Hawley S. L., Kowalski A. F., 2010, *AJ*, **140**, 1402
- Houdebine E. R., Mullan D. J., Paletou F., Gebran M., 2016, *ApJ*, **822**, 97
- Houdebine E. R., Mullan D. J., Bercu B., Paletou F., Gebran M., 2017, *VizieR Online Data Catalog*, p. J/ApJ/837/96
- Howell S. B., et al., 2014, *PASP*, **126**, 398
- Huang C. X., et al., 2020, *Research Notes of the AAS*, **4**, 204
- Irwin J. M., et al., 2011, *ApJ*, **742**, 123
- Jackson R. J., Jeffries R. D., 2013, *MNRAS*, **431**, 1883
- Jeffers S. V., et al., 2018, *A&A*, **614**, A76
- Jenkins J. S., Ramsey L. W., Jones H. R. A., Pavlenko Y., Gallardo J., Barnes J. R., Pinfield D. J., 2009, *ApJ*, **704**, 975
- Jenkins J. M., et al., 2016, in Chiozzi G., Guzman J. C., eds, *Society of Photo-Optical Instrumentation Engineers (SPIE) Conference Series Vol. 9913, Software and Cyberinfrastructure for Astronomy IV*. p. 99133E, doi:10.1117/12.2233418
- Kimani R., Schmidt S. J., Angus R., Cruz K. L., Faherty J. K., Rice E., 2019, *AJ*, **157**, 231
- Kimani R., et al., 2021, *AJ*, **161**, 277
- Kiraga M., 2012, *Acta Astron.*, **62**, 67
- Kiraga M., Stepień K., 2007, *Acta Astron.*, **57**, 149
- Koch D. G., et al., 2010, *ApJ*, **713**, L79
- Kouwenhoven M. B. N., Brown A. G. A., Goodwin S. P., Portegies Zwart S. F., Kaper L., 2009, *A&A*, **493**, 979



- Kowalski A. F., Hawley S. L., Holtzman J. A., Wisniewski J. P., Hilton E. J., 2010, *ApJ*, **714**, L98
- Kruse E. A., Berger E., Knapp G. R., Laskar T., Gunn J. E., Loomis C. P., Lupton R. H., Schlegel D. J., 2010, *ApJ*, **722**, 1352
- Lee K.-G., Berger E., Knapp G. R., 2010, *ApJ*, **708**, 1482
- Lépine S., Gaidos E., 2011, *AJ*, **142**, 138
- Lépine S., Hilton E. J., Mann A. W., Wilde M., Rojas-Ayala B., Cruz K. L., Gaidos E., 2013, *AJ*, **145**, 102
- Maehara H., Notsu Y., Notsu S., Namekata K., Honda S., Ishii T. T., Nogami D., Shibata K., 2017, *PASJ*, **69**, 41
- Magaudda E., Stelzer B., Covey K. R., Raetz S., Matt S. P., Scholz A., 2020, *A&A*, **638**, A20
- Mamajek E. E., Hillenbrand L. A., 2008, *ApJ*, **687**, 1264
- Medina A. A., Charbonneau D., Winters J. G., Irwin J., Mink J., 2022, *The Astrophysical Journal*, 928, 185
- Mercer A., Stamatellos D., 2020, *A&A*, **633**, A116
- Messina S., Naves R., Medhi B. J., 2016, *New Astron.*, **48**, 5
- Messina S., et al., 2017, *A&A*, **600**, A83
- Morin J., Donati J. F., Petit P., Delfosse X., Forveille T., Jardine M. M., 2010, *MNRAS*, **407**, 2269
- Newton E. R., Irwin J., Charbonneau D., Berta-Thompson Z. K., Dittmann J. A., 2016, *ApJ*, **821**, L19
- Newton E. R., Irwin J., Charbonneau D., Berlind P., Calkins M. L., Mink J., 2017, *ApJ*, **834**, 85
- Newton E. R., Mondrik N., Irwin J., Winters J. G., Charbonneau D., 2018, *AJ*, **156**, 217
- Notsu Y., et al., 2019, *The Astrophysical Journal*, 876, 58
- Pallavicini R., Golub L., Rosner R., Vaiana G. S., Ayres T., Linsky J. L., 1981, *ApJ*, **248**, 279
- Queiroz A. B. A., et al., 2018, *MNRAS*, **476**, 2556
- Queiroz A. B. A., et al., 2023, *A&A*, **673**, A155
- Radick R. R., Lockwood G. W., Skiff B. A., Baliunas S. L., 1998, *ApJS*, **118**, 239
- Raetz S., Stelzer B., Damasso M., Scholz A., 2020, *A&A*, **637**, A22
- Rajpurohit A. S., et al., 2012, *A&A*, **545**, A85
- Rajpurohit A. S., Reylé C., Allard F., Homeier D., Schultheis M., Bessell M. S., Robin A. C., 2013, *A&A*, **556**, A15
- Rajpurohit A. S., Kumar V., Srivastava M. K., Allard F., Homeier D., Dixit V., Patel A., 2020, *MNRAS*, **492**, 5844
- Reid N., Hawley S. L., Mateo M., 1995, *MNRAS*, **272**, 828
- Reiners A., Basri G., 2007, *ApJ*, **656**, 1121
- Reiners A., Joshi N., Goldman B., 2012, *AJ*, **143**, 93
- Reiners A., Schüssler M., Passetger V. M., 2014, *ApJ*, **794**, 144
- Renzini A., et al., 1996, *ApJ*, **465**, L23+
- Ricker G. R., et al., 2015, *Journal of Astronomical Telescopes, Instruments, and Systems*, **1**, 014003
- Riedel A. R., Alam M. K., Rice E. L., Cruz K. L., Henry T. J., 2017, *ApJ*, **840**, 87
- Rodríguez Martínez R., Lopez L. A., Shappee B. J., Schmidt S. J., Jayasinghe T., Kochanek C. S., Aucht K., Holoiën T. W. S., 2020, *ApJ*, **892**, 144
- Schöfer P., et al., 2019, *A&A*, **623**, A44
- Schöfer P., et al., 2022, *A&A*, **663**, A68
- Srivastava M. K., Jangra M., Dixit V., Munjal B. S., Arora H., Mavani T., 2018, in *Proc. SPIE*. p. 107024I, doi:10.1117/12.2309306
- Srivastava M. K., Kumar V., Dixit V., Patel A., Jangra M., Rajpurohit A. S., Mathur S. N., 2021, *Experimental Astronomy*, Stelzer B., Bogner M., Magaudda E., Raetz S., 2022, *A&A*, **665**, A30
- Suárez Mascareño A., et al., 2018, *A&A*, **612**, A89
- Vidotto A. A., et al., 2014, *MNRAS*, **441**, 2361
- Walkowicz L. M., Hawley S. L., 2009, *AJ*, **137**, 3297
- Walkowicz L. M., Hawley S. L., West A. A., 2004, *PASP*, **116**, 1105
- Walkowicz L. M., et al., 2011, *AJ*, **141**, 50
- West A. A., Hawley S. L., 2008, *PASP*, **120**, 1161
- West A. A., Hawley S. L., Bochanski J. J., Covey K. R., Reid I. N., Dhital S., Hilton E. J., Masuda M., 2008, *AJ*, **135**, 785
- West A. A., Hawley S. L., Bochanski J. J., Covey K. R., Burgasser A. J., 2009, in Mamajek E. E., Soderblom D. R., Wyse R. F. G., eds, Vol. 258, *The Ages of Stars*. pp 327–336 (arXiv:0812.1223), doi:10.1017/S1743921309031986
- West A. A., Weisenburger K. L., Irwin J., Berta-Thompson Z. K., Charbonneau D., Dittmann J., Pineda J. S., 2015, *ApJ*, **812**, 3
- Wright N. J., Drake J. J., Mamajek E. E., Henry G. W., 2011, *ApJ*, **743**, 48
- Wright N. J., Newton E. R., Williams P. K. G., Drake J. J., Yadav R. K., 2018, *MNRAS*, **479**, 2351
- Yang H., et al., 2017, *ApJ*, **849**, 36
- Zechmeister M., Kürster M., 2009, *A&A*, **496**, 577

# 1 Supplementary Material

## 1.1 Appendix-I

The figure shows the spectral times series (panel a), photometric light curves from TESS and Kepler/K2 databases (panel b), EWs light curves for  $H\alpha$  and  $H\beta$  emissions (panel c) and their computed fractional structure functions (SFs) (panel d) for each of the sources observed with MFOSC-P instrument on PRL 1.2m telescope at Mt. Abu. Source ID, spectral type, and rotation period are also mentioned at the top of the panel (a). Data for  $H\alpha$  and  $H\beta$  are shown in red circles and black triangles, respectively. The Y-axis (ordinate) of panel (a) is in arbitrary units of flux. Y-axes of panel (c) are in units of  $\text{\AA}$  for  $H\alpha$  (left) and  $H\beta$  (right). Y-axes of the panel (d) are the fractional structure function (SF) for  $H\alpha$  (left) and  $H\beta$  (right). Units of X-axes (abscissa) of the panel (a), (c), and (d) are given at the bottom of these plots. The X-axis of the panel (b) - photometric light curves - is in units of days, and Y-axis is in arbitrary units of flux. See Fig.4 of the main text also for these units. For some sources, either light curves were not found or rotation periods could not be determined, and/or  $H\beta$  emission was not covered. Thus, these data are not presented for some of the sources.

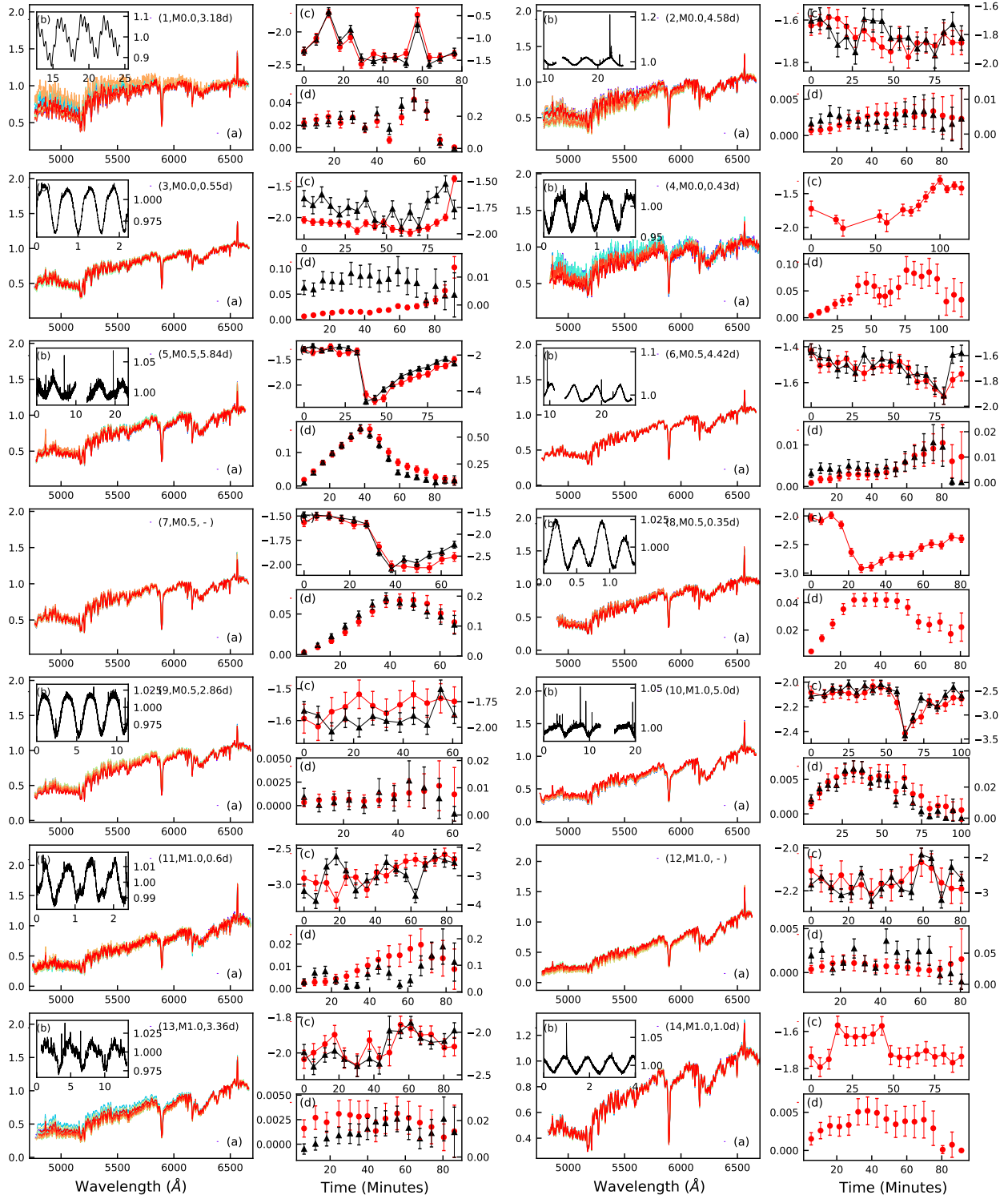


Figure 1: The figure shows the spectral times series (panel a), photometric light curves from TESS and Kepler/K2 databases (panel b), EWs light curves for H $\alpha$  and H $\beta$  emissions (panel c) and their computed fractional structure functions (SFs) (panel d) for each of the sources (full caption is given in the Appendix-I text).

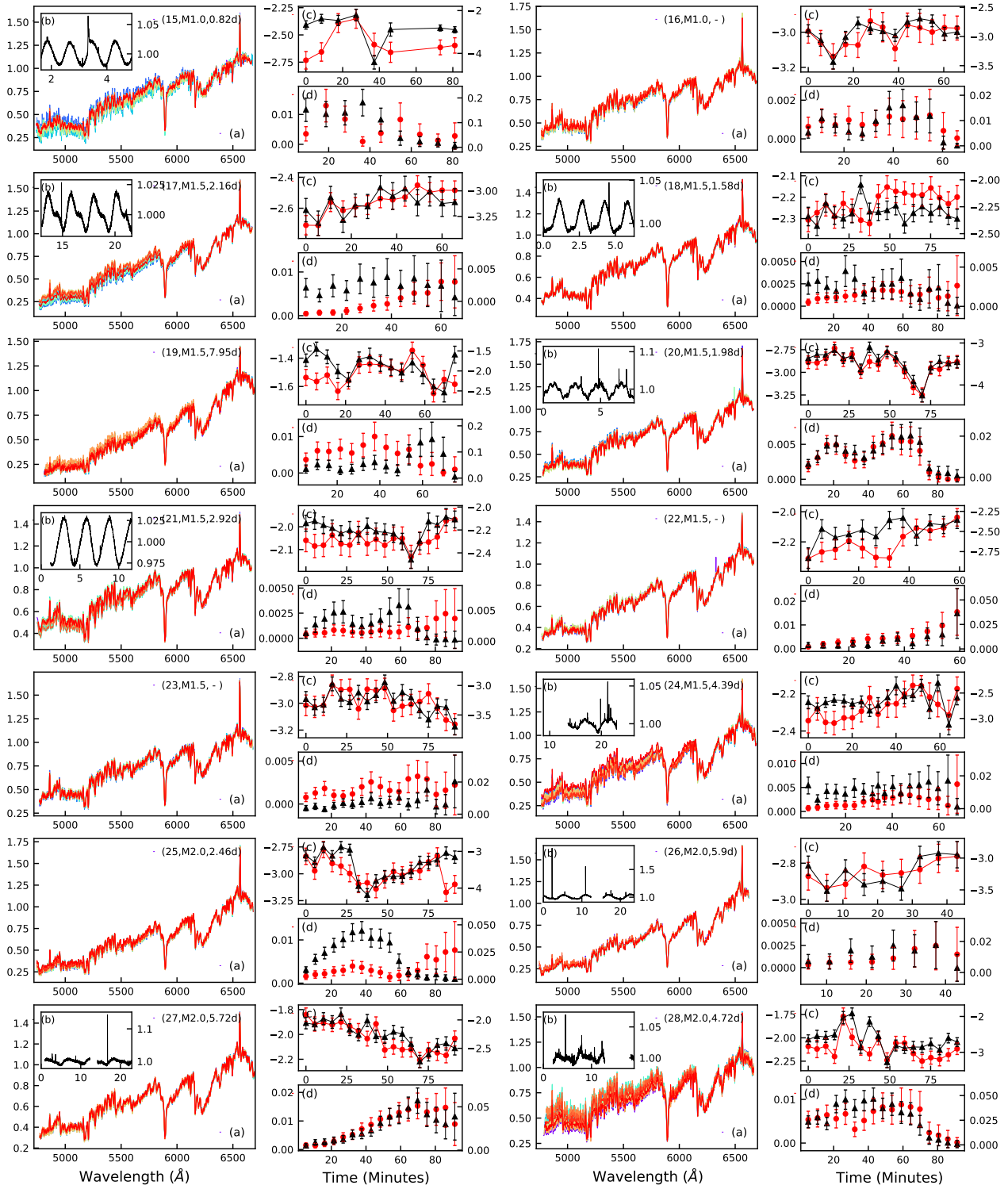


Figure 1: Continue...

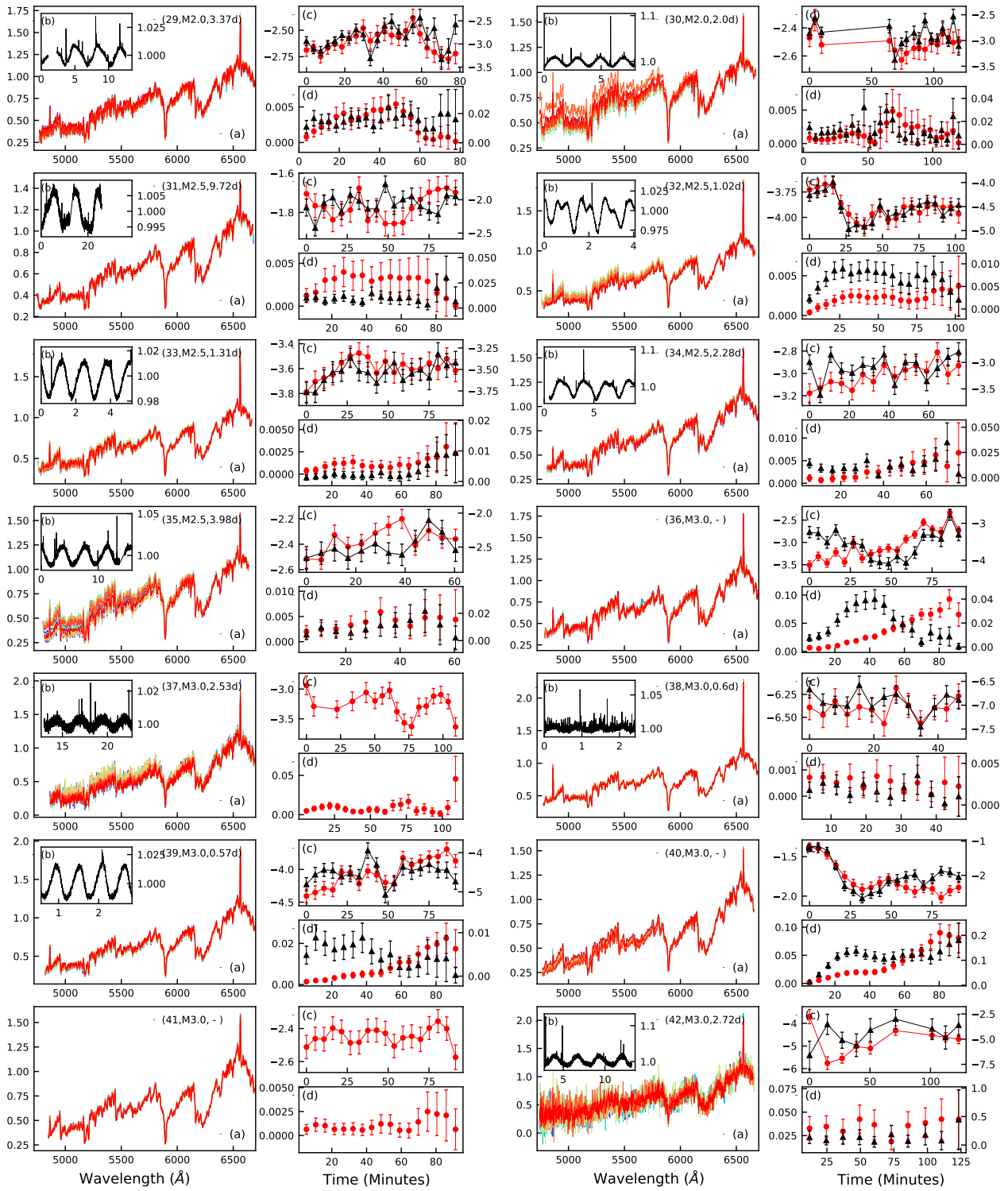


Figure 1: Continue...

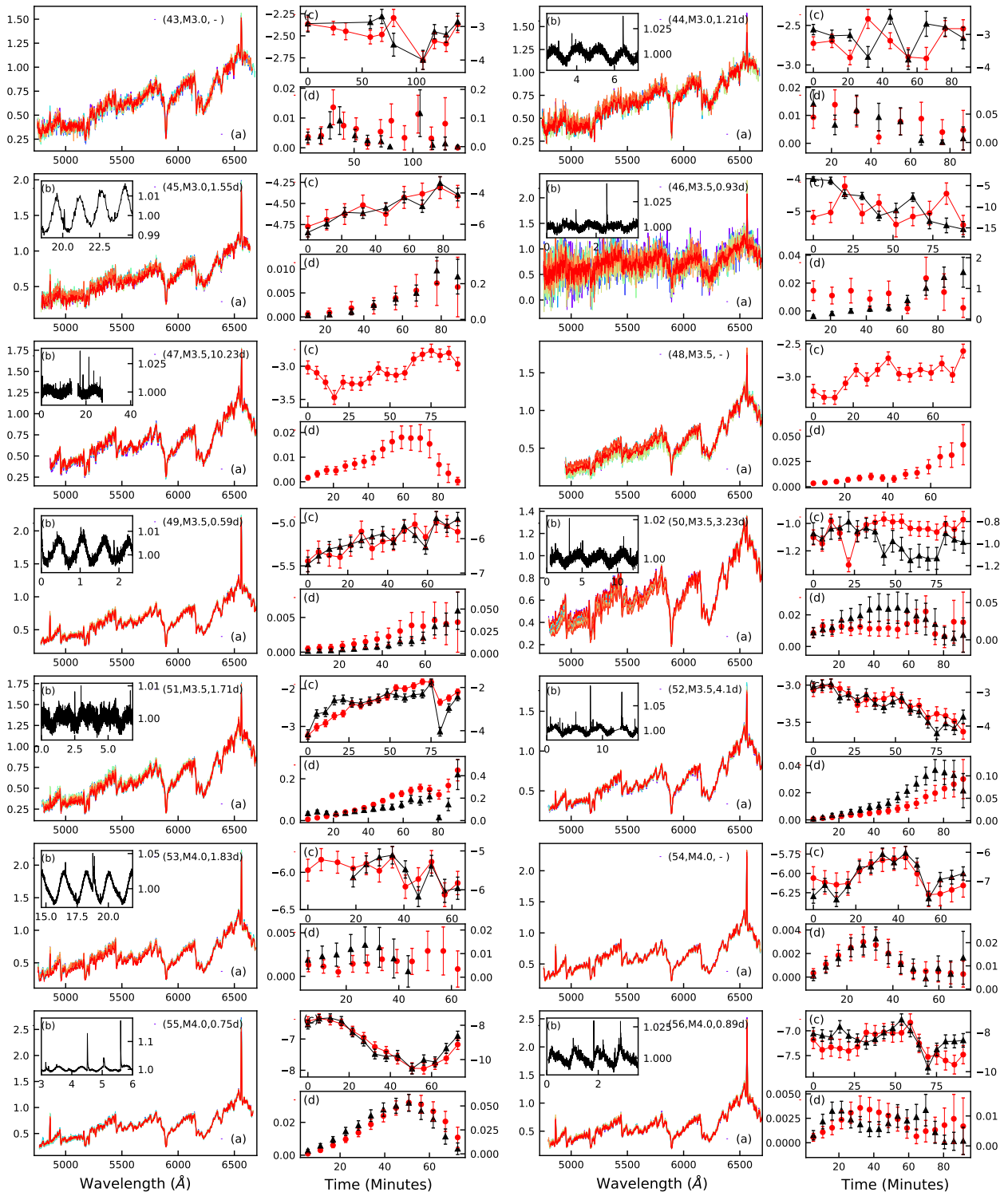


Figure 1: Continue...

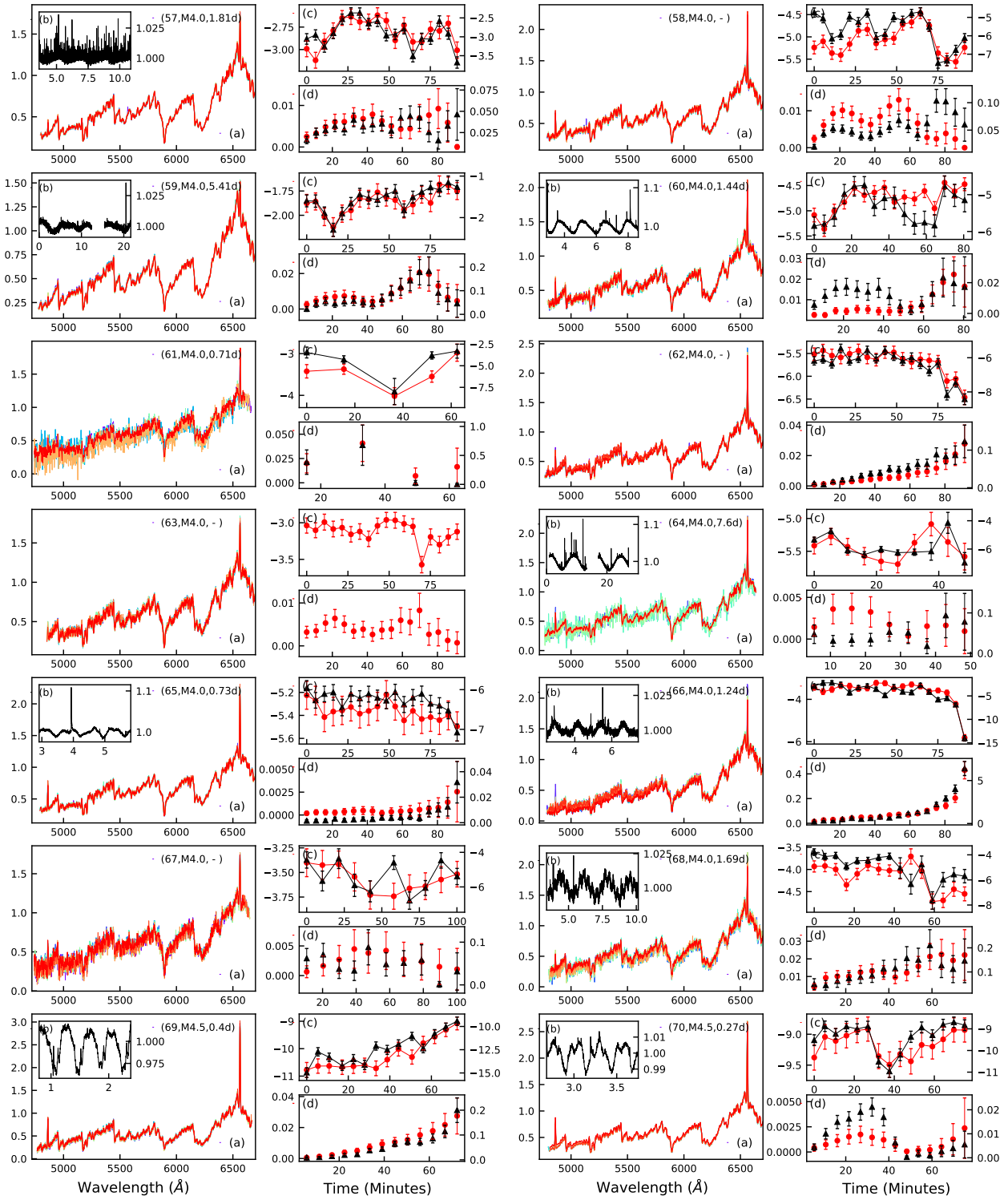


Figure 1: Continue...

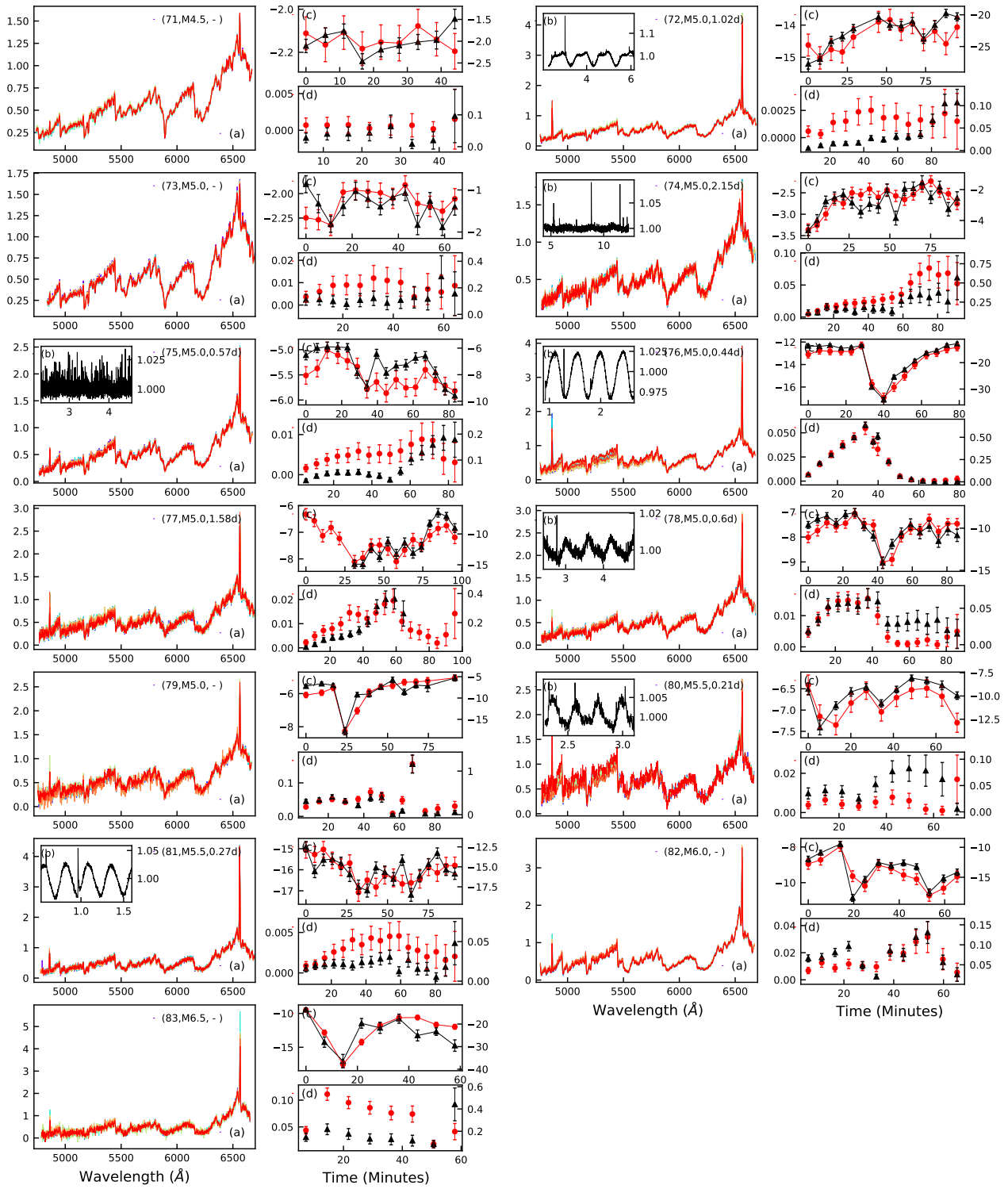


Figure 1: Continue...



## 1.2 Appendix-II

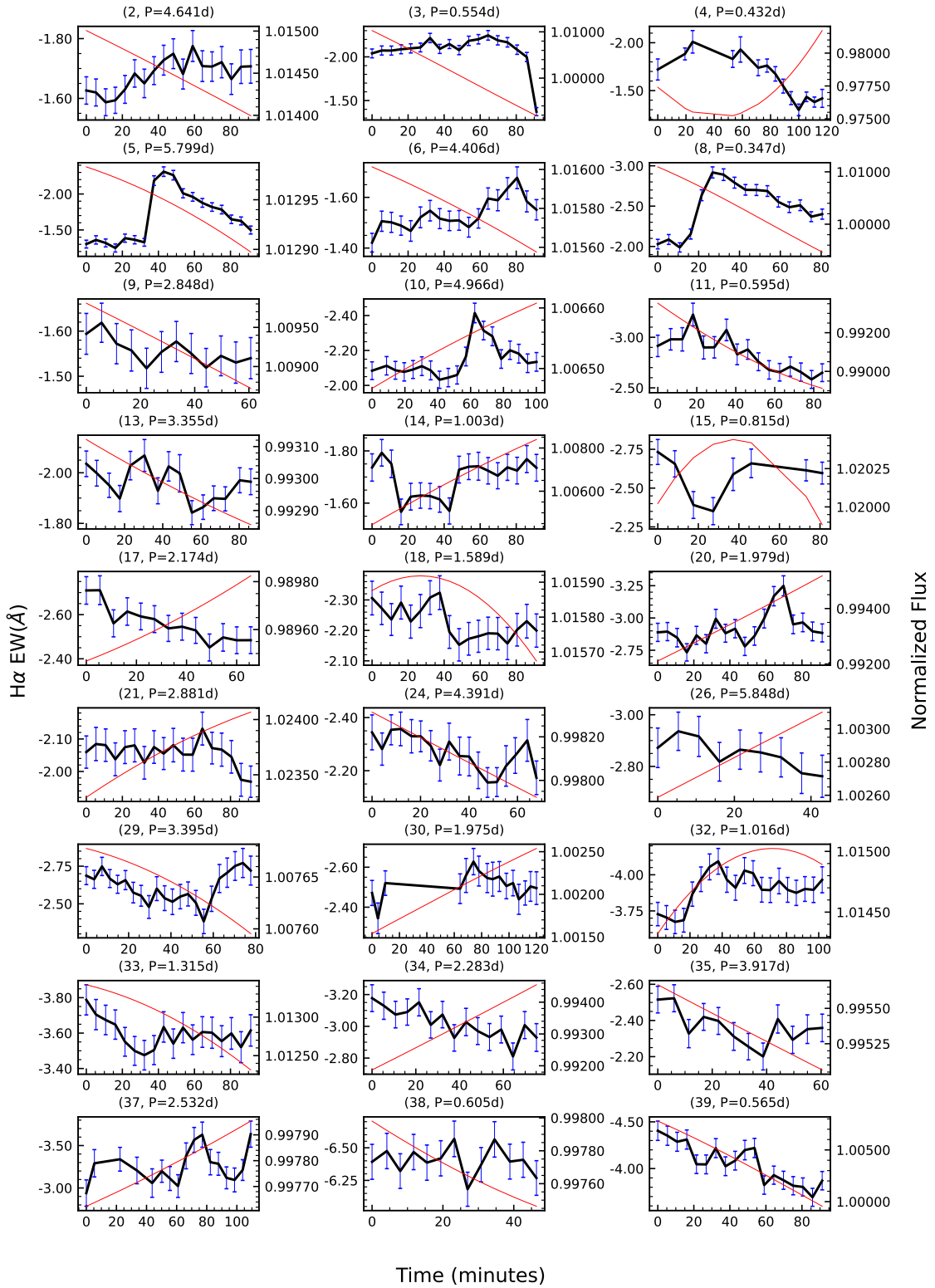


Figure 2: The figure shows the H $\alpha$  Equivalent Width (EW) light curve (black data points) and corresponding extrapolated photometric light curve (red line; from TESS and Kepler/K2 databases). Source ID and rotation period are also mentioned at the top of each panel. The left Y-axis of each panel is the H $\alpha$  EW in the units of Å and the right Y-axis is the full phase mean normalized flux. The X-axis of each panel is the time in units of minutes, taking reference as the starting of our spectroscopic monitoring observation.

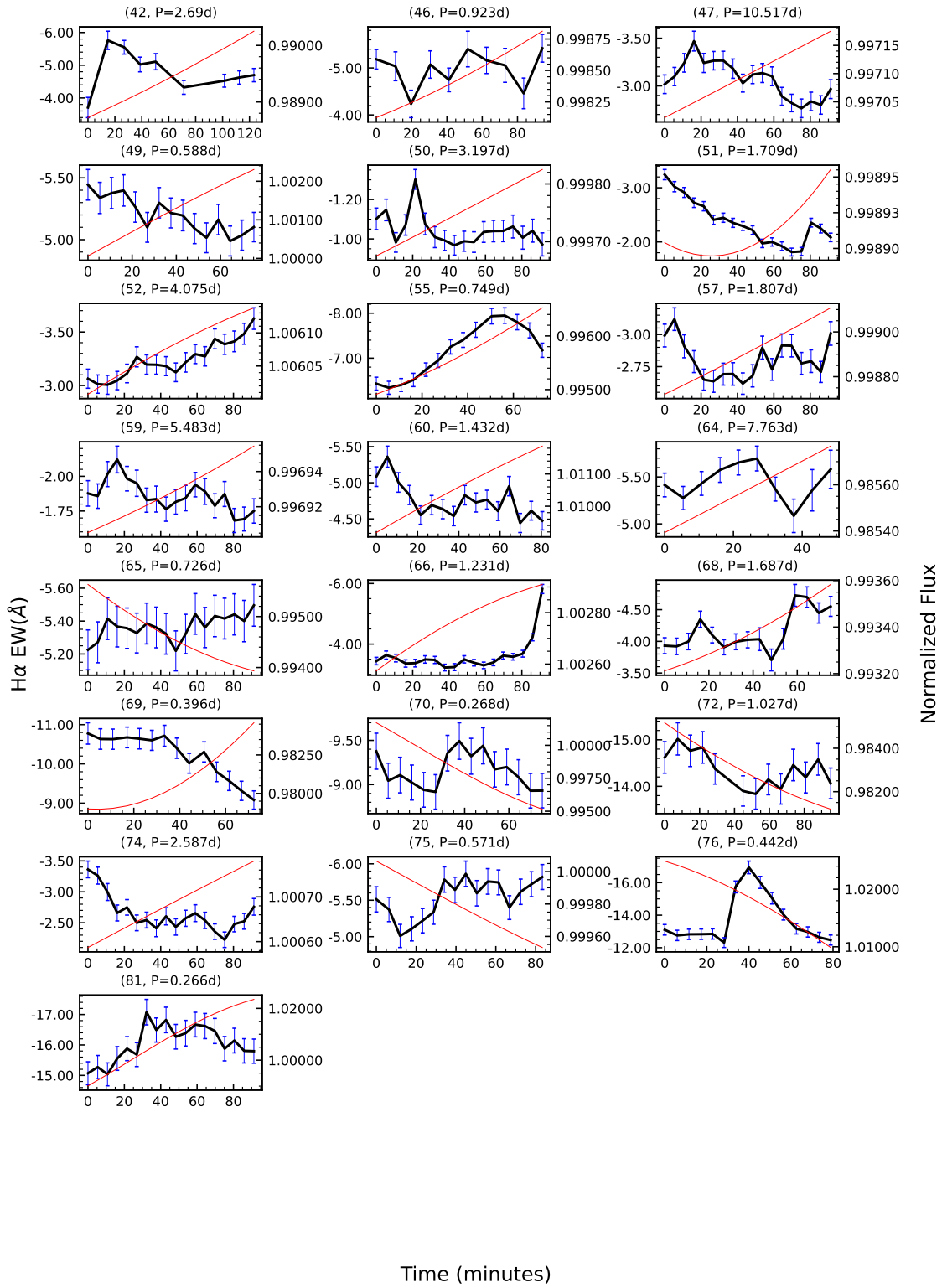


Figure 2: Continue...

### 1.3 Appendix-III

Table 1: Observation details of the sources of this study along with the derived stellar parameters. V band magnitudes are taken from the SIMBAD database. The spectral types are mostly taken from [Lépine et al. \(2013\)](#), and [Jeffers et al. \(2018\)](#), except for six sources where we have derived the spectral class. These sources are marked with (★).

Source ID	Source name	Spectral type	Magnitude (V-band)	Date of observation (UT)	Frame exposure time × No. of frames (s)	log g (cm s <sup>-2</sup> )	T <sub>eff</sub> (K)
1	PM J03332+4615S	M0.0	13.09	2020-12-29.602	300sx14	5.0	3900
2	PM J03416+5513	M0.0	-	2021-02-01.600	300sx18	5.0	3800
3	PM J07151+1555	M0.0	11.37	2021-01-30.754	300sx18	5.0	4000
4	PM J23083-1524	M0.0	10.87	2020-11-26.563	300sx14	4.5	3900
5	PM J03322+4914S	M0.5	11.94	2021-02-03.680	300sx18	5.0	3700
6	PM J04595+0147	M0.5	10.11	2021-01-31.618	300sx18	5.0	3900
7	PM J10143+2104	M0.5	10.08	2020-12-29.882	300sx13	5.0	3800
8	PM J19026+3231	M0.5	11.57	2021-03-23.963	300sx16	5.0	3700
9	PM J23060+6355	M0.5	10.96	2020-12-27.599	300sx12	5.0	3700
10	PM J06310+5002	M1.0	-	2021-01-31.711	300sx19	5.0	3700
11	PM J08317+0545	M1.0	11.93	2021-01-30.854	300sx16	5.0	3800
12	PM J09193+6203	M1.0	-	2021-03-08.811	300sx16	5.5	3600
13	PM J12576+3513E	M1.0	-	2020-03-20.846	300sx15	5.0	3600
14	PM J15238+5609	M1.0	11.68	2021-03-22.832	300sx18	5.0	3800
15	PM J15581+4927	M1.0	-	2020-05-06.890	450sx8	5.5	3600
16	PM J04376-0229	M1.0	10.59	2020-12-29.755	300sx13	5.0	3600
17	PM J00428+3532	M1.5	-	2020-12-29.679	300sx13	5.0	3500
18	PM J05402+1239	M1.5	11.35	2021-03-02.606	300sx18	5.0	3700
19	PM J06262+2349	M1.5	11.82	2021-03-26.681	300sx15	5.0	3500
20	PM J07295+3556	M1.5	11.88	2021-02-03.787	300sx18	5.0	3600
21	PM J13007+1222	M1.5	9.75	2021-01-31.905	300sx18	4.5	3900
22	PM J15416+1828	M1.5	12.32	2021-02-01.007	300sx12	5.0	3600
23	PM J16220+2250	M1.5	12.12	2021-03-25.850	300sx18	5.0	3700
24	PM J22387-2037	M1.5	9.08	2020-12-02.626	200sx18	5.0	3600
25	PM J04284+1741	M2.0	12.12	2021-02-01.683	300sx18	5.0	3500
26	PM J06212+4414	M2.0	-	2021-01-31.825	300sx9	5.0	3500
27	PM J11201-1029	M2.0	11.25	2021-03-23.772	300sx18	5.0	3500
28	PM J13518+1247	M2.0	12.25	2021-02-01.940	300sx18	5.0	3800
29	PM J15218+2058	M2.0	10.00	2021-03-08.973	200sx22	5.0	3600
30	PM J16170+5516	M2.0	9.46	2020-05-06.752	200sx16	5.0	3600
31	PM J06596+0545	M2.5	12.50	2021-02-01.764	300sx18	5.0	3500
32	PM J09177+4612	M2.5	11.58	2021-01-28.857	300sx20	5.0	3500
33	PM J10043+5023	M2.5	-	2021-02-01.851	300sx18	5.0	3500
34	PM J11519+0731	M2.5	12.42	2021-03-08.902	300sx15	5.0	3500
35	PM J15557+6840	M2.5	11.97	2020-05-22.902	300sx12	5.0	3400
36	PM J04333+2359	M3.0	12.66	2021-02-02.597	300sx18	4.5	3500
37	PM J05091+1527	M3.0	-	2021-02-02.685	300sx17	5.0	3400
38	PM J05337+0156	M3.0	11.50	2020-11-27.854	200sx13	5.0	3400
39	PM J05547+1055	M3.0	-	2021-03-27.613	300sx18	4.5	3500
40	PM J07319+3613S	M3.0	-	2021-03-25.611	300sx18	5.0	3400
41	PM J07349+1445	M3.0	11.15	2021-02-02.786	300sx18	5.0	3400
42	PM J11529+3554★	M3.0	13.69	2020-05-21.751	600sx9	5.0	3300
43	PM J12355+2439★	M3.0	13.43	2020-03-08.784	600sx10	5.0	3500
44	PM J13352+1714★	M3.0	13.19	2020-05-24.730	600sx9	5.0	3600
45	PM J14137+4618★	M3.0	13.14	2020-05-21.873	600sx9	5.0	3400
46	PM J04238+1455	M3.5	13.35	2020-11-26.785	500sx10	4.5	3500
47	PM J09302+2630	M3.5	-	2021-02-02.870	300sx18	4.5	3400
48	PM J09557+3521	M3.5	-	2021-02-02.967	300sx15	5.0	3300
49	PM J12485+4933	M3.5	12.51	2021-02-03.977	300sx15	5.0	3400

Table 1: continue...

Source ID	Source name	Spectral type	Magnitude (V-band)	Date of observation (UT)	Frame exposure time × No. of frames (s)	log g (cm s <sup>-2</sup> )	T <sub>eff</sub> (K)
50	PM J12490+6606	M3.5	-	2021-03-26.764	300sx18	4.5	3500
51	PM J13417+5815	M3.5	12.54	2021-03-23.871	300sx18	5.0	3300
52	PM J16591+2058	M3.5	12.45	2021-03-26.892	300sx18	5.0	3400
53	PM J00325+0729	M4.0	12.80	2020-11-27.723	300sx12	4.5	3200
54	PM J01593+5831	M4.0	12.15	2020-11-27.786	300sx14	5.0	3200
55	PM J02088+4926	M4.0	12.45	2020-12-02.827	300sx14	5.0	3300
56	PM J05062+0439	M4.0	13.46	2021-02-12.597	300sx18	4.0	3200
57	PM J06000+0242	M4.0	11.31	2021-03-26.601	300sx18	5.0	3200
58	PM J07033+3441	M4.0	-	2021-02-12.685	300sx18	5.0	3200
59	PM J07100+3831	M4.0	11.52	2021-03-27.697	300sx18	5.0	3100
60	PM J09161+0153	M4.0	13.03	2021-02-24.75	300sx16	5.0	3300
61	PM J10357+0215*	M4.0	13.57	2020-05-22.665	600sx5	5.0	3400
62	PM J10360+0507	M4.0	12.64	2021-02-23.784	300sx18	5.0	3300
63	PM J11033+1337	M4.0	-	2021-03-24.744	300sx18	5.0	3300
64	PM J11118+3332S	M4.0	-	2021-02-24.827	300sx10	5.0	3300
65	PM J12156+5239	M4.0	12.56	2021-02-12.863	300sx18	5.0	3400
66	PM J13536+7737	M4.0	-	2021-02-12.971	300sx18	5.0	3100
67	PM J14165-0725*	M4.0	13.76	2020-05-22.806	600sx10	4.5	3400
68	PM J15126+4543	M4.0	13.33	2021-02-24.975	300sx15	5.0	3200
69	PM J05243-1601	M4.5	13.57	2020-12-02.899	300sx14	4.0	3000
70	PM J13317+2916	M4.5	12.02	2021-02-24.900	300sx15	5.0	3200
71	PM J17199+2630W	M4.5	11.34	2020-05-21.956	300sx9	5.0	3200
72	PM J01033+6221	M5.0	13.21	2020-11-28.675	400sx13	4.0	3000
73	PM J02002+1303	M5.0	12.30	2021-02-23.597	300sx13	5.0	3100
74	PM J06579+6219	M5.0	-	2021-02-24.600	300sx18	4.0	3000
75	PM J07364+0704	M5.0	13.24	2020-12-02.970	300sx16	5.5	3000
76	PM J09449-1220	M5.0	13.65	2020-11-27.914	300sx15	4.0	3200
77	PM J12142+0037	M5.0	-	2021-02-23.879	300sx18	4.0	3100
78	PM J13005+0541	M5.0	-	2021-02-23.972	300sx17	4.5	3100
79	PM J20298+0941	M5.0	-	2020-11-28.570	400sx12	5.0	3000
80	PM J12332+0901	M5.5	12.47	2020-12-29.950	300sx11	4.0	3200
81	PM J17338+1655	M5.5	14.38	2021-03-25.944	300sx18	5.5	3000
82	PM J10564+0700	M6.0	13.51	2020-11-27.989	300sx12	4.0	3000
83	PM J11055+4331	M6.5	14.45	2020-12-31.011	400sx9	5.5	3000

Table 2: The derived variability parameters for  $H\alpha$  and  $H\beta$  emission lines for the sources of this study, along with the activity strengths ( $\log_{10}(L_{H\alpha}/L_{bol})$  and  $\log_{10}(L_{H\beta}/L_{bol})$ ). The  $p$ -values are determined from the  $\chi^2$  minimisation of EW light curves. The sources which are characterize as variable are marked with ( $\star$ ).

Source ID	Source name	emission line	Median H $\alpha$ EW H $\beta$ EW	Minimum H $\alpha$ EW H $\beta$ EW	Maximum H $\alpha$ EW H $\beta$ EW	$\Delta$ H $\alpha$ EW H $\beta$ EW	RMS H $\alpha$ EW H $\beta$ EW	Mean $\log_{10}(L_{H\alpha}/L_{bol})$ $\log_{10}(L_{H\beta}/L_{bol})$	P-value H $\alpha$ H $\beta$
1	PM J03332+4615S*	H $\alpha$	-2.333 ± 0.065	-1.717 ± 0.062	-2.492 ± 0.061	0.775 ± 0.087	0.232 ± 0.022	-3.883	0.0000
		H $\beta$	-1.372 ± 0.085	-0.413 ± 0.091	-1.590 ± 0.086	1.177 ± 0.125	0.349 ± 0.031	-4.199	0.0000
2	PM J03416+5513	H $\alpha$	-1.688 ± 0.047	-1.587 ± 0.045	-1.775 ± 0.052	0.188 ± 0.068	0.051 ± 0.012	-3.984	0.2298
		H $\beta$	-1.818 ± 0.085	-1.690 ± 0.076	-1.947 ± 0.087	0.258 ± 0.116	0.080 ± 0.020	-3.981	0.4134
3	PM J07151+1555*	H $\alpha$	-2.094 ± 0.052	-1.372 ± 0.046	-2.246 ± 0.055	0.874 ± 0.072	0.183 ± 0.012	-3.854	0.0000
		H $\beta$	-1.755 ± 0.076	-1.525 ± 0.077	-1.942 ± 0.081	0.417 ± 0.111	0.110 ± 0.019	-3.905	0.0062
4	PM J23083-1524*	H $\alpha$	-1.698 ± 0.110	-1.298 ± 0.061	-2.010 ± 0.117	0.711 ± 0.132	0.220 ± 0.025	-3.980	0.0000
		H $\beta$	-	-	-	-	-	-	-
5	PM J03322+4914S*	H $\alpha$	-1.637 ± 0.059	-1.249 ± 0.056	-2.311 ± 0.066	1.062 ± 0.087	0.346 ± 0.015	-3.960	0.0000
		H $\beta$	-2.431 ± 0.121	-1.486 ± 0.111	-4.612 ± 0.141	3.127 ± 0.179	0.979 ± 0.032	-3.766	0.0000
6	PM J04595+0147*	H $\alpha$	-1.516 ± 0.039	-1.421 ± 0.037	-1.677 ± 0.043	0.256 ± 0.057	0.061 ± 0.010	-4.033	0.0012
		H $\beta$	-1.673 ± 0.067	-1.574 ± 0.065	-1.916 ± 0.068	0.342 ± 0.094	0.091 ± 0.016	-4.030	0.0083
7	PM J10143+2104*	H $\alpha$	-1.817 ± 0.044	-1.499 ± 0.041	-2.033 ± 0.048	0.533 ± 0.063	0.219 ± 0.013	-3.973	0.0000
		H $\beta$	-2.239 ± 0.078	-1.560 ± 0.066	-2.787 ± 0.082	1.226 ± 0.105	0.456 ± 0.022	-3.940	0.0000
8	PM J19026+3231*	H $\alpha$	-2.532 ± 0.064	-1.988 ± 0.057	-2.918 ± 0.069	0.930 ± 0.090	0.290 ± 0.016	-3.815	0.0000
		H $\beta$	-	-	-	-	-	-	-
9	PM J23060+6355	H $\alpha$	-1.552 ± 0.045	-1.518 ± 0.045	-1.619 ± 0.043	0.101 ± 0.062	0.029 ± 0.013	-4.057	0.9234
		H $\beta$	-1.902 ± 0.091	-1.629 ± 0.089	-2.042 ± 0.085	0.413 ± 0.123	0.100 ± 0.027	-4.046	0.1749
10	PM J06310+5002*	H $\alpha$	-2.112 ± 0.053	-2.032 ± 0.049	-2.415 ± 0.056	0.382 ± 0.075	0.096 ± 0.013	-3.907	0.0000
		H $\beta$	-2.541 ± 0.086	-2.364 ± 0.086	-3.426 ± 0.102	1.062 ± 0.133	0.255 ± 0.023	-3.884	0.0000
11	PM J08317+0545*	H $\alpha$	-2.855 ± 0.096	-2.583 ± 0.088	-3.225 ± 0.112	0.642 ± 0.143	0.173 ± 0.026	-3.781	0.0000
		H $\beta$	-2.799 ± 0.221	-2.322 ± 0.248	-3.882 ± 0.259	1.560 ± 0.359	0.484 ± 0.065	-3.823	0.0000
12	PM J09193+6203	H $\alpha$	-2.164 ± 0.066	-2.067 ± 0.066	-2.213 ± 0.069	0.146 ± 0.096	0.041 ± 0.017	-3.865	0.9796
		H $\beta$	-2.816 ± 0.178	-1.923 ± 0.186	-3.238 ± 0.217	1.315 ± 0.286	0.382 ± 0.052	-3.776	0.0000
13	PM J12576+3513E*	H $\alpha$	-1.965 ± 0.051	-1.842 ± 0.047	-2.068 ± 0.063	0.226 ± 0.079	0.066 ± 0.014	-3.928	0.0479
		H $\beta$	-2.217 ± 0.085	-1.889 ± 0.074	-2.405 ± 0.090	0.517 ± 0.117	0.164 ± 0.028	-3.923	0.0000
14	PM J15238+5609*	H $\alpha$	-1.726 ± 0.051	-1.567 ± 0.049	-1.793 ± 0.051	0.226 ± 0.071	0.068 ± 0.012	-3.994	0.0112
		H $\beta$	-	-	-	-	-	-	-
15	PM J15581+4927*	H $\alpha$	-2.606 ± 0.068	-2.352 ± 0.087	-2.733 ± 0.080	0.381 ± 0.119	0.125 ± 0.032	-3.897	0.0162
		H $\beta$	-2.743 ± 0.139	-2.208 ± 0.270	-4.415 ± 0.316	2.207 ± 0.416	0.639 ± 0.110	-3.998	0.0000
16	PM J04376-0229	H $\alpha$	-2.994 ± 0.068	-2.936 ± 0.067	-3.137 ± 0.072	0.201 ± 0.098	0.060 ± 0.020	-3.720	0.6793
		H $\beta$	-2.911 ± 0.160	-2.695 ± 0.161	-3.437 ± 0.120	0.743 ± 0.201	0.185 ± 0.035	-3.753	0.0010
17	PM J00428+3532	H $\alpha$	-2.545 ± 0.061	-2.451 ± 0.061	-2.711 ± 0.065	0.260 ± 0.089	0.078 ± 0.018	-3.878	0.0655
		H $\beta$	-3.116 ± 0.128	-2.968 ± 0.116	-3.317 ± 0.120	0.349 ± 0.167	0.103 ± 0.035	-3.911	0.6763
18	PM J05402+1239	H $\alpha$	-2.215 ± 0.054	-2.153 ± 0.053	-2.324 ± 0.055	0.171 ± 0.077	0.053 ± 0.013	-3.931	0.4400
		H $\beta$	-2.309 ± 0.080	-2.046 ± 0.084	-2.429 ± 0.088	0.383 ± 0.122	0.082 ± 0.021	-4.028	0.4803
19	PM J06262+2349*	H $\alpha$	-1.520 ± 0.057	-1.346 ± 0.059	-1.649 ± 0.060	0.303 ± 0.084	0.079 ± 0.016	-4.039	0.0232
		H $\beta$	-1.804 ± 0.206	-1.452 ± 0.171	-2.538 ± 0.237	1.086 ± 0.292	0.297 ± 0.054	-3.976	0.0018
20	PM J07295+3556*	H $\alpha$	-2.892 ± 0.070	-2.733 ± 0.067	-3.249 ± 0.078	0.515 ± 0.102	0.122 ± 0.018	-3.775	0.0000
		H $\beta$	-3.381 ± 0.133	-3.103 ± 0.123	-4.253 ± 0.151	1.149 ± 0.195	0.268 ± 0.034	-3.766	0.0000
21	PM J13007+1222	H $\alpha$	-2.063 ± 0.050	-1.969 ± 0.048	-2.132 ± 0.051	0.164 ± 0.070	0.037 ± 0.012	-3.986	0.8947
		H $\beta$	-2.192 ± 0.074	-2.088 ± 0.075	-2.460 ± 0.075	0.371 ± 0.106	0.086 ± 0.018	-4.090	0.1217
22	PM J15416+1828*	H $\alpha$	-2.218 ± 0.065	-2.037 ± 0.058	-2.311 ± 0.065	0.274 ± 0.087	0.088 ± 0.018	-3.965	0.0086
		H $\beta$	-2.475 ± 0.115	-2.333 ± 0.117	-2.831 ± 0.128	0.498 ± 0.173	0.132 ± 0.036	-4.054	0.2102
23	PM J16220+2250	H $\alpha$	-3.012 ± 0.075	-2.866 ± 0.076	-3.156 ± 0.079	0.290 ± 0.109	0.082 ± 0.019	-3.761	0.2604
		H $\beta$	-3.268 ± 0.130	-2.946 ± 0.123	-3.698 ± 0.139	0.751 ± 0.185	0.181 ± 0.031	-3.781	0.0051
24	PM J22387-2037	H $\alpha$	-2.269 ± 0.061	-2.156 ± 0.056	-2.357 ± 0.063	0.202 ± 0.084	0.065 ± 0.015	-3.869	0.2155
		H $\beta$	-2.660 ± 0.118	-2.302 ± 0.155	-3.125 ± 0.196	0.823 ± 0.250	0.190 ± 0.040	-3.847	0.0360
25	PM J04284+1741*	H $\alpha$	-2.976 ± 0.079	-2.775 ± 0.076	-3.172 ± 0.083	0.398 ± 0.113	0.107 ± 0.019	-3.859	0.0103
		H $\beta$	-3.296 ± 0.142	-2.881 ± 0.150	-4.188 ± 0.171	1.307 ± 0.228	0.370 ± 0.039	-3.976	0.0000
26	PM J06212+4414	H $\alpha$	-2.854 ± 0.076	-2.762 ± 0.082	-2.936 ± 0.074	0.174 ± 0.110	0.055 ± 0.027	-3.841	0.8049
		H $\beta$	-3.188 ± 0.160	-2.923 ± 0.180	-3.517 ± 0.162	0.594 ± 0.242	0.223 ± 0.062	-3.917	0.0634
27	PM J11201-1029*	H $\alpha$	-2.033 ± 0.059	-1.841 ± 0.054	-2.206 ± 0.062	0.365 ± 0.082	0.111 ± 0.014	-3.976	0.0000
		H $\beta$	-2.254 ± 0.104	-1.899 ± 0.110	-2.733 ± 0.108	0.834 ± 0.154	0.223 ± 0.027	-4.045	0.0000
28	PM J13518+1247*	H $\alpha$	-2.118 ± 0.062	-1.771 ± 0.091	-2.248 ± 0.072	0.478 ± 0.115	0.112 ± 0.020	-3.997	0.0071
		H $\beta$	-2.680 ± 0.132	-1.915 ± 0.152	-3.277 ± 0.153	1.363 ± 0.216	0.327 ± 0.037	-4.059	0.0000
29	PM J15218+2058*	H $\alpha$	-2.615 ± 0.060	-2.383 ± 0.081	-2.771 ± 0.097	0.388 ± 0.126	0.099 ± 0.018	-3.866	0.0351
		H $\beta$	-2.864 ± 0.216	-2.430 ± 0.182	-3.331 ± 0.213	0.901 ± 0.280	0.244 ± 0.039	-3.943	0.0000
30	PM J16170+5516	H $\alpha$	-2.513 ± 0.064	-2.344 ± 0.077	-2.628 ± 0.066	0.284 ± 0.101	0.062 ± 0.019	-3.900	0.7030
		H $\beta$	-2.909 ± 0.096	-2.533 ± 0.140	-3.380 ± 0.176	0.847 ± 0.224	0.214 ± 0.039	-3.974	0.0020
31	PM J06596+0545	H $\alpha$	-1.775 ± 0.062	-1.675 ± 0.061	-1.858 ± 0.062	0.182 ± 0.087	0.065 ± 0.015	-4.062	0.2529
		H $\beta$	-2.069 ± 0.120	-1.767 ± 0.123	-2.424 ± 0.118	0.657 ± 0.170	0.141 ± 0.030	-4.139	0.1106
32	PM J09177+4612*	H $\alpha$	-3.899 ± 0.085	-3.674 ± 0.081	-4.093 ± 0.089	0.419 ± 0.120	0.117 ± 0.019	-3.693	0.0049
		H $\beta$	-4.515 ± 0.134	-3.989 ± 0.124	-4.974 ± 0.137	0.986 ± 0.185	0.258 ± 0.030	-3.744	0.0000
33	PM J10043+5023	H $\alpha$	-3.600 ± 0.088	-3.475 ± 0.083	-3.788 ± 0.085	0.313 ± 0.119	0.077 ± 0.020	-3.739	0.5912
		H $\beta$	-3.528 ± 0.121	-3.322 ± 0.133	-3.768 ± 0.117	0.446 ± 0.177	0.118 ± 0.030	-3.874	0.4600
34	PM J11519+0731	H $\alpha$	-3.009 ± 0.083	-2.810 ± 0.085	-3.177 ± 0.084	0.367 ± 0.120	0.096 ± 0.023	-3.858	0.1592
		H $\beta$	-3.051 ± 0.150	-2.805 ± 0.177	-3.617 ± 0.142	0.812 ± 0.227	0.221 ± 0.042	-4.023	0.0063
35	PM J15557+6840	H $\alpha$	-2.355 ± 0.076	-2.201 ± 0.074	-2.523 ± 0.075	0.322 ± 0.105	0.092 ± 0.022	-3.907	0.0708
		H $\beta$	-2.552 ± 0.157	-2.104 ± 0.157	-2.662 ± 0.163	0.558 ± 0.226	0.159 ± 0.048	-3.996	0.3764
36	PM J04333+2359*	H $\alpha$	-3.156 ± 0.086	-2.333 ± 0.072	-3.511 ± 0.094	1.178 ± 0.118	0.329 ± 0.020	-3.846	0.0000
		H $\beta$	-3.518 ± 0.155	-2.772 ± 0.146	-4.090 ± 0.158	1.319 ± 0.215	0.358 ± 0.038	-3.948	0.0000
37	PM J05091+1527*	H $\alpha$	-3.211 ± 0.122	-2.940 ± 0.155	-3.635 ± 0.154	0.695 ± 0.219	0.199 ± 0.037	-3.829	0.0150
		H $\beta$	-	-	-	-	-	-	-



Table 2: continues...

Source ID	Source name	emission line	Median	Minimum	Maximum	$\Delta$	RMS	Mean	P-value
			H $\alpha$ EW H $\beta$ EW	H $\alpha$ EW H $\beta$ EW	H $\alpha$ EW H $\beta$ EW	H $\alpha$ EW H $\beta$ EW	H $\alpha$ EW H $\beta$ EW	H $\alpha$ EW H $\beta$ EW	$\log_{10}(L_{H\alpha}/L_{bol})$ $\log_{10}(L_{H\beta}/L_{bol})$
77	PM J12142+0037*	H $\alpha$	-7.256 $\pm$ 0.233	-6.326 $\pm$ 0.214	-8.113 $\pm$ 0.241	1.787 $\pm$ 0.322	0.492 $\pm$ 0.057	-3.808	0.0000
		H $\beta$	-12.128 $\pm$ 0.765	-6.575 $\pm$ 0.681	-14.916 $\pm$ 0.666	8.341 $\pm$ 0.952	2.693 $\pm$ 0.193	-4.087	0.0000
78	PM J13005+0541*	H $\alpha$	-7.589 $\pm$ 0.208	-7.055 $\pm$ 0.195	-9.026 $\pm$ 0.232	1.971 $\pm$ 0.303	0.502 $\pm$ 0.056	-3.646	0.0000
		H $\beta$	-9.765 $\pm$ 0.518	-8.155 $\pm$ 0.482	-14.109 $\pm$ 0.660	5.954 $\pm$ 0.817	1.433 $\pm$ 0.147	-3.889	0.0000
79	PM J20298+0941*	H $\alpha$	-5.622 $\pm$ 0.158	-5.053 $\pm$ 0.171	-8.264 $\pm$ 0.222	3.212 $\pm$ 0.280	0.870 $\pm$ 0.062	-3.813	0.0000
		H $\beta$	-7.182 $\pm$ 0.336	-5.312 $\pm$ 0.699	-17.770 $\pm$ 0.861	12.458 $\pm$ 1.109	3.106 $\pm$ 0.245	-4.076	0.0000
80	PM J12332+0901*	H $\alpha$	-6.706 $\pm$ 0.210	-6.411 $\pm$ 0.233	-7.350 $\pm$ 0.232	0.939 $\pm$ 0.329	0.322 $\pm$ 0.072	-3.872	0.0123
		H $\beta$	-9.305 $\pm$ 0.355	-8.079 $\pm$ 0.329	-13.386 $\pm$ 0.791	5.307 $\pm$ 0.856	1.433 $\pm$ 0.201	-4.216	0.0000
81	PM J17338+1655*	H $\alpha$	-16.011 $\pm$ 0.394	-15.034 $\pm$ 0.376	-17.078 $\pm$ 0.419	2.044 $\pm$ 0.563	0.580 $\pm$ 0.096	-3.526	0.0019
		H $\beta$	-15.474 $\pm$ 0.780	-12.478 $\pm$ 0.651	-18.510 $\pm$ 0.799	6.032 $\pm$ 1.030	1.537 $\pm$ 0.182	-4.066	0.0000
82	PM J10564+0700*	H $\alpha$	-9.604 $\pm$ 0.303	-7.968 $\pm$ 0.276	-10.721 $\pm$ 0.322	2.753 $\pm$ 0.425	0.726 $\pm$ 0.090	-3.746	0.0000
		H $\beta$	-13.160 $\pm$ 0.499	-9.466 $\pm$ 0.433	-18.432 $\pm$ 0.572	8.966 $\pm$ 0.717	2.485 $\pm$ 0.155	-4.100	0.0000
83	PM J11055+4331*	H $\alpha$	-11.761 $\pm$ 0.357	-9.479 $\pm$ 0.288	-17.546 $\pm$ 0.478	8.067 $\pm$ 0.558	2.260 $\pm$ 0.147	-3.850	0.0000
		H $\beta$	-23.353 $\pm$ 1.646	-13.665 $\pm$ 0.782	-36.401 $\pm$ 2.937	22.736 $\pm$ 3.039	6.440 $\pm$ 0.806	-4.258	0.0000

Table 3: Derived rotation periods and star-spot filling factors of the objects of this study using TESS and Kepler/K2 light curves. The rotation periods from the literature survey are also mentioned with references and remark (if any). The observing details from TESS and Kepler/K2 archives and computed mean values of FLI for H $\alpha$  and H $\beta$  emissions from the spectral time series are also mentioned. The flaring sources (as per FLI criteria) during the spectroscopy observations are marked with ( $\star$ ) in the source-name column. In the third column (mission/year/author) column, the notation ‘T’ represents TESS sector and a ‘K’ represents K2 campaign.

Source ID	Source name	Mission/Year/Author	Exposure time (s)	Rotation period (days)	Rotation Period from literature <sup>b</sup> (days)	Ref. <sup>a</sup>	T <sub>spot</sub> (K)	Filling factor %	Mean FLI H $\alpha$	Mean FLI H $\beta$
1	PM J03332+4615S $\star$	T-18/2019/QLP	1800	3.160	-	-	3192	36	10.40 $\pm$ 1.72	2.65 $\pm$ 0.95
2	PM J03416+5513 $\star$	T-19/2019/SPOC	120	4.641	8 <sup>1</sup>	4	3145	6.2	6.97 $\pm$ 0.62	4.50 $\pm$ 0.45
3	PM J07151+1555 $\star$	T-33/2020/SPOC	120	0.554	0.555	6	3239	9.6	12.05 $\pm$ 1.83	4.67 $\pm$ 0.42
4	PM J23083-1524	T-42/2021/SPOC	20	0.432	0.431	6	3192	8.9	6.17 $\pm$ 1.25	-
5	PM J03322+4914S $\star$	T-18/2019/SPOC	120	5.799	5.947	9	3097	5	7.09 $\pm$ 1.59	6.23 $\pm$ 2.72
6	PM J04595+0147 $\star$	T-32/2020/SPOC	120	4.406	4.414	6	3192	7.1	6.75 $\pm$ 0.43	4.63 $\pm$ 0.50
7	PM J10143+2104 $\star$	-	-	-	7.861	6	3145	-	8.00 $\pm$ 1.36	5.28 $\pm$ 1.25
8	PM J19026+3231	T-14/2019/SPOC	120	0.347	3.545 <sup>2</sup>	9	3097	7.6	11.91 $\pm$ 2.38	-
9	PM J23060+6355 $\star$	T-24/2020/SPOC	120	2.848	2.831	5	3097	11.3	6.96 $\pm$ 0.66	4.33 $\pm$ 0.55
10	PM J06310+5002 $\star$	T-20/2019/SPOC	120	4.966	15.25 <sup>2</sup>	9	3097	2.6	8.68 $\pm$ 1.04	6.32 $\pm$ 0.81
11	PM J08317+0545 $\star$	T-07/2019/SPOC	120	0.595	1.4755 <sup>2</sup>	6	3145	4.6	10.06 $\pm$ 0.96	4.13 $\pm$ 1.06
12	PM J09193+6203 $\star$	T-21/2020/SPOC	120	-	2.992	9	3048	3	8.22 $\pm$ 0.60	4.03 $\pm$ 0.74
13	PM J12576+3513E $\star$	T-22/2020/SPOC	120	3.355	3.170	5	3048	7.7	7.95 $\pm$ 0.79	5.09 $\pm$ 0.76
14	PM J15238+5609	T-24/2020/SPOC	120	1.003	-	-	3145	5	7.26 $\pm$ 0.64	-
15	PM J15581+4927 $\star$	T-24/2020/SPOC	120	0.815	4.492 <sup>2</sup>	9	3048	8.5	9.17 $\pm$ 1.28	3.97 $\pm$ 0.92
16	PM J04376-0229	T-05/2018/QLP	1800	-	4.890	1	3048	-	11.35 $\pm$ 0.65	6.48 $\pm$ 0.98
17	PM J00428+3532 $\star$	T-17/2019/SPOC	120	2.174	2.170	4	2998	6.4	10.02 $\pm$ 0.97	6.04 $\pm$ 0.76
18	PM J05402+1239 $\star$	T-06/2018/SPOC	120	1.589	0.6125 <sup>2</sup>	5	3097	6.8	9.36 $\pm$ 0.77	6.02 $\pm$ 0.71
19	PM J06262+2349	K/2014/K2	1800	8.059	7.890	4	2998	5.8	5.20 $\pm$ 0.46	2.81 $\pm$ 0.81
20	PM J07295+3556 $\star$	T-20/2019/SPOC	120	1.979	1.970	1	3048	7.2	11.36 $\pm$ 1.07	7.40 $\pm$ 0.60
21	PM J13007+1222	T-23/2020/SPOC	120	2.881	2.886	6	3192	9.5	8.20 $\pm$ 0.57	6.15 $\pm$ 0.65
22	PM J15416+1828 $\star$	T-24/2020/TESS-SPOC	1800	-	-	-	3048	-	8.39 $\pm$ 0.74	5.90 $\pm$ 0.70
23	PM J16220+2250	T-25/2020/QLP	1800	-	-	-	3097	7.2	10.78 $\pm$ 0.72	8.12 $\pm$ 0.86
24	PM J22387-2037 $\star$	T-42/2021/SPOC	120	4.391	4.230	4	3048	3.7	7.76 $\pm$ 0.63	4.92 $\pm$ 0.82
25	PM J04284+1741 $\star$	K-13/2017/K2	1800	2.449	2.440	4	2998	10.6	10.10 $\pm$ 0.91	6.08 $\pm$ 0.88
26	PM J06212+4414	T-20/2019/SPOC	120	5.848	5.728	9	2998	16.1	9.33 $\pm$ 0.69	4.92 $\pm$ 0.75
27	PM J11201-1029 $\star$	T-09/2019/SPOC	120	5.652	-	-	2998	3.4	7.05 $\pm$ 0.64	4.93 $\pm$ 0.84
28	PM J13518+1247 $\star$	T-23/2020/SPOC	120	-	-	-	3145	2.2	7.70 $\pm$ 1.02	5.61 $\pm$ 0.95
29	PM J15218+2058 $\star$	T-24/2020/SPOC	120	3.395	3.383	5	3048	3.5	9.27 $\pm$ 1.24	5.85 $\pm$ 1.27
30	PM J16170+5516 $\star$	T-25/2020/SPOC	120	1.975	-	-	3048	3.7	8.79 $\pm$ 0.70	6.55 $\pm$ 0.98
31	PM J06596+0545 $\star$	T-33/2020/TESS-SPOC	600	10.331	-	-	2998	2.5	5.99 $\pm$ 0.46	3.94 $\pm$ 0.55
32	PM J09177+4612 $\star$	T-21/2020/SPOC	120	1.016	0.56 <sup>3</sup>	4	2998	7.4	13.47 $\pm$ 1.16	9.70 $\pm$ 1.14
33	PM J10043+5023 $\star$	T-21/2020/SPOC	120	1.315	1.313	5	2998	5.9	11.19 $\pm$ 0.79	7.30 $\pm$ 0.81
34	PM J11519+0731 $\star$	T-22/2020/SPOC	120	2.283	2.291	6	2998	10.1	9.59 $\pm$ 0.70	6.46 $\pm$ 1.23
35	PM J15557+6840	T-40/2021/SPOC	120	3.917	3.930	8	2948	4.4	7.73 $\pm$ 0.56	4.43 $\pm$ 0.55
36	PM J04333+2359 $\star$	-	-	-	-	-	2998	-	8.19 $\pm$ 0.62	6.46 $\pm$ 0.69
37	PM J05091+1527	T-32/2020/SPOC	120	2.532	2.540	10	2948	1.2	7.01 $\pm$ 0.92	-
38	PM J05337+0156 $\star$	T-32/2020/SPOC	20	0.605	2.510 <sup>4</sup>	2	2948	1.3	18.46 $\pm$ 1.40	12.84 $\pm$ 1.31
39	PM J05547+1055 $\star$	T-33/2020/SPOC	120	0.565	1.13 <sup>2</sup>	9	2998	5.5	11.63 $\pm$ 1.03	7.73 $\pm$ 1.78
40	PM J07319+3613S $\star$	T-20/2019/QLP	1800	-	3.69	2	2948	9.3	4.37 $\pm$ 0.63	3.10 $\pm$ 0.88
41	PM J07349+1445	T-07/2019/SPOC	120	-	20.08	9	2948	2.3	5.80 $\pm$ 0.42	-
42	PM J11529+3554	T-22/2020/SPOC	120	2.690	2.69	4	2896	6	8.36 $\pm$ 1.85	1.08 $\pm$ 0.53
43	PM J12355+2439	-	-	-	-	-	2998	-	7.79 $\pm$ 0.56	3.82 $\pm$ 0.49
44	PM J13352+1714 $\star$	T-23/2020/SPOC	120	1.213	-	-	3048	2.2	9.02 $\pm$ 1.49	4.75 $\pm$ 1.50
45	PM J14137+4618 $\star$	T-23/2020/TESS-SPOC	1800	1.536	-	-	2948	4.4	13.28 $\pm$ 1.55	5.31 $\pm$ 2.45
46	PM J04238+1455 $\star$	T-32/2020/SPOC	120	0.923	-	-	2998	1.1	5.65 $\pm$ 1.18	2.52 $\pm$ 0.94
47	PM J09302+2630	T-21/2020/SPOC	120	10.517	10.68	11	2948	1.3	6.36 $\pm$ 0.64	-
48	PM J09557+3521	T-21/2020/SPOC	120	-	-	-	2896	0.5	6.83 $\pm$ 0.59	-
49	PM J12485+4933 $\star$	T-15/2019/SPOC	120	0.588	4.063 <sup>2</sup>	9	2948	2.1	11.95 $\pm$ 1.02	9.57 $\pm$ 1.04
50	PM J12490+6606	T-22/2020/SPOC	120	3.197	5.55 <sup>4</sup>	14	2998	1	2.32 $\pm$ 0.35	1.39 $\pm$ 0.27
51	PM J13417+5815 $\star$	T-16/2019/SPOC	120	1.709	-	-	2896	0.9	5.66 $\pm$ 0.84	3.72 $\pm$ 1.07
52	PM J16591+2058 $\star$	T-25/2020/SPOC	120	4.075	-	-	2948	4.2	6.92 $\pm$ 0.59	4.86 $\pm$ 0.82

a : References- 1. [Messina et al. \(2017\)](#), 2. [Houdebine et al. \(2016\)](#), 3. [Vidotto et al. \(2014\)](#), 4. [Magaudda et al. \(2020\)](#), 5. [Newton et al. \(2017\)](#), 6. [Kiraga \(2012\)](#), 7. [Schöfer et al. \(2019\)](#), 8. [Stelzer et al. \(2022\)](#), 9. [Rodríguez Martínez et al. \(2020\)](#), 10. [Raetz et al. \(2020\)](#), 11. [Newton et al. \(2016\)](#), 12. [Günther et al. \(2020\)](#), 13. [Newton et al. \(2018\)](#), 14. [Houdebine et al. \(2017\)](#).

b: Sources having different rotation periods from this study, computed with the following method: 1. This was estimated by the empirical relation between Chromospheric activity and rotation period, 2. This was estimated by using All Sky Automated Survey (ASAS) photometry data (having low cadence; mostly one data point per day), 3. This was estimated by Hungarian-made Automated Telescope Network (HATNet) survey photometry data (they studied 1568 stars), 4. This was estimated with the help of  $v\text{-sin}i$  and the radius of the star, where the star’s radius was calculated using empirical relation, 5. [Messina et al. \(2016\)](#) estimated this rotation period using their own photometry observation of this previously known visual binary stars, 6. This was estimated by using photometry data from MEarth (having cadence of 30 minutes; they studied 387 stars).



Table 3: Continue...

Source ID	Source name	Mission/Year/Author	Exposure time (s)	Rotation period (days)	Rotation Period from literature <sup>b</sup> (days)	Ref. <sup>a</sup>	$T_{spot}$ (K)	Filling factor %	Mean FLI H $\alpha$	Mean FLI H $\beta$
53	PM J00325+0729	T-42/2021/SPOC	120	1.820	3.355,0.925 <sup>a</sup>	1	2845	11.3	9.89 $\pm$ 0.63	6.41 $\pm$ 0.80
54	PM J01593+5831	-	-	-	4.144	9	2845	-	9.41 $\pm$ 0.72	7.90 $\pm$ 0.90
55	PM J02088+4926*	T-18/2019/SPOC	120	0.749	0.748	7	2896	4.1	15.00 $\pm$ 1.37	11.00 $\pm$ 1.28
56	PM J05062+0439	T-05/2018/SPOC	120	0.889	0.889	6	2845	4	10.80 $\pm$ 0.87	9.28 $\pm$ 1.42
57	PM J06000+0242*	T-33/2020/SPOC	20	1.807	1.809	5	2845	1.1	4.89 $\pm$ 0.49	3.72 $\pm$ 0.67
58	PM J07033+3441*	T-20/2019/SPOC	120	-	0.889	11	2845	3.4	8.59 $\pm$ 0.66	6.95 $\pm$ 0.87
59	PM J07100+3831	T-20/2019/SPOC	120	5.483	5.593	5	2792	1.7	2.44 $\pm$ 0.22	1.39 $\pm$ 0.33
60	PM J09161+0153*	T-08/2019/SPOC	120	1.432	4.308 <sup>2</sup>	9	2896	8.2	8.61 $\pm$ 0.77	6.44 $\pm$ 1.39
61	PM J10357+0215	K-14/2017/K2	1800	0.707	-	-	2948	4	6.56 $\pm$ 1.40	1.98 $\pm$ 0.89
62	PM J10360+0507	-	-	-	6.843	9	2896	-	10.42 $\pm$ 0.62	8.04 $\pm$ 1.56
63	PM J11033+1337	T-22/2020/SPOC	120	-	34.42	5	2896	0.5	6.03 $\pm$ 0.64	-
64	PM J11118+3332S*	T-22/2020/SPOC	120	7.763	7.770	5	2896	9.3	10.39 $\pm$ 1.28	6.93 $\pm$ 3.01
65	PM J12156+5239	T-22/2020/SPOC	120	0.726	4.891 <sup>2</sup>	9	2948	3.4	12.16 $\pm$ 0.94	10.23 $\pm$ 0.94
66	PM J13536+7737*	T-41/2021/SPOC	120	1.231	1.231	5	2792	2	6.78 $\pm$ 1.44	3.09 $\pm$ 2.02
67	PM J14165-0725*	-	-	-	-	-	2948	-	7.61 $\pm$ 0.68	3.50 $\pm$ 1.13
68	PM J15126+4543*	T-24/2020/SPOC	120	1.687	1.686	5	2845	3.9	6.64 $\pm$ 0.80	4.22 $\pm$ 1.41
69	PM J05243-1601*	T-32/2020/SPOC	120	0.396	0.401	1	2739	15.9	11.90 $\pm$ 1.15	10.24 $\pm$ 1.73
70	PM J13317+2916	T-23/2020/SPOC	120	0.268	0.268	11	2845	3.5	14.97 $\pm$ 0.87	13.42 $\pm$ 2.09
71	PM J17199+2630W	T-25/2020/SPOC	120	-	19.808	5	2845	5.7	4.20 $\pm$ 0.27	2.27 $\pm$ 0.57
72	PM J01033+6221	T-24/2020/SPOC	120	1.027	1.024	5	2739	20.1	16.70 $\pm$ 1.19	18.53 $\pm$ 3.05
73	PM J02002+1303	-	-	-	0.199	11	2792	-	2.62 $\pm$ 0.27	1.10 $\pm$ 0.64
74	PM J06579+6219	T-20/2019/SPOC	120	2.587	54.5 <sup>6</sup>	5	2739	1.6	3.12 $\pm$ 0.42	1.57 $\pm$ 0.98
75	PM J07364+0704*	T-34/2021/SPOC	20	0.571	0.996 <sup>6</sup>	11	2739	0.6	6.20 $\pm$ 0.60	5.85 $\pm$ 1.13
76	PM J09449-1220*	T-35/2021/SPOC	120	0.442	0.442	6	2845	14.9	14.35 $\pm$ 1.51	16.30 $\pm$ 7.87
77	PM J12142+0037*	K-102/2016/K2SFF	1800	1.584	1.583	5	2792	5.1	7.77 $\pm$ 0.67	6.41 $\pm$ 2.18
78	PM J13005+0541*	T-23/2020/SPOC	120	0.600	0.6	5	2792	2.9	9.82 $\pm$ 0.88	7.06 $\pm$ 1.57
79	PM J20298+0941*	-	-	-	0.257	5	2739	-	7.88 $\pm$ 1.32	5.05 $\pm$ 2.44
80	PM J12332+0901	T-23/2020/SPOC	120	0.207	-	-	2845	1.5	6.39 $\pm$ 0.37	7.62 $\pm$ 1.28
81	PM J17338+1655*	T-26/2020/SPOC	120	0.266	0.266	5	2739	18.5	15.48 $\pm$ 1.28	9.33 $\pm$ 1.15
82	PM J10564+0700*	K-14/2017/K2SFF	1800	-	-	-	2739	6.2	6.53 $\pm$ 0.71	10.03 $\pm$ 2.96
83	PM J11055+4331*	T-21/2020/QLP	1800	-	0.780	3	2739	-	9.58 $\pm$ 1.62	5.63 $\pm$ 1.37

Table 4: The derived rotation periods and star-spot filling factors for 31 sources of Lee et al. (2010). The  $T_{eff}$  values for these sources are estimated from  $T_{eff}$  versus spectral type relation given in Rajpurohit et al. (2013).

Source name	Mission/Year/ Author	Exposure time (s)	Rotation period (days)	Rotation Period from literature (days)	Ref.	$T_{eff}$ (K)	$T_{spot}$ (K)	Filling factor %
G99-049	T-33/2020/SPOC	120	1.805	1.809	5	3100	2792	1.2
LHS1723	T-32/2020/SPOC	20	-	88.5	5	3100	2792	0.5
L449-1	T-32/2020/SPOC	120	1.296	-	-	3100	2792	2
GL285	T-34/2021/SPOC	120	2.770	2.77	3	3000	2739	4.52
2MASSWJ1013426-275958	T-09/2019/SPOC	120	1.163	-	-	2900	2685	3.8
DENIS-PJ213422.2-431610	T-28/2020/SPOC	120	-	-	-	2800	2630	0.5
2MASSJ02591181+0046468	T-04/2018/SPOC	120	-	-	-	2800	2630	0.8
2MASSJ02534448-7959133	T-39/2021/SPOC	120	-	-	-	2800	2630	1.8
2MASSJ00244419-2708242	T-29/2020/SPOC	120	0.945	0.9432	12	2800	2630	11.3
2MASSJ00045753-1709369	T-29/2020/SPOC	120	0.192	0.192157	12	2800	2630	1.9
2MASSJ20021341-5425558	T-27/2020/SPOC	120	0.692	-	-	2800	2630	4.4
LP844-25	T-35/2021/SPOC	120	-	-	-	2800	2630	2.9
2MASSJ23373831-1250277	T-42/2021/SPOC	120	-	4.9705	12	2800	2630	7.3
2MASSWJ1012065-304926	T-36/2021/SPOC	120	0.724	-	-	2800	2630	3.5
LP731-47	T-36/2021/SPOC	120	-	0.588	13	2800	2630	3.6
2MASSJ23155449-0627462	T-42/2021/SPOC	120	0.127	-	-	2800	2630	4.1
GJ3622	T-09/2019/SPOC	120	-	-	-	2700	2575	0.9
2MASSJ05023867-3227500	T-32/2020/SPOC	120	0.759	-	-	2700	2575	5
2MASSJ02141251-0357434	T-31/2020/SPOC	120	2.296	2.33	13	2700	2575	6
2MASSJ10031918-0105079	T-08/2019/TESS-SPOC	1800	0.213	-	-	2700	2575	21.8
2MASSJ13092185-2330350	T-10/2019/SPOC	120	-	-	-	2700	2575	2.8
2MASSWJ1420544-361322	T-11/2019/SPOC	120	-	-	-	2700	2575	8.6
2MASSJ09522188-1924319	T-35/2021/SPOC	120	0.909	-	-	2600	2519	41.6
2MASSJ04291842-3123568	T-32/2020/SPOC	120	0.907	-	-	2600	2519	3.6
2MASSJ23062928-0502285	K-19/2018/K2	1800	-	3.29	7	2600	2519	-
2MASSJ03313025-3042383	T-31/2020/SPOC	120	1.043	-	-	2600	2519	3.9
2MASSJ04351612-1606574	T-32/2020/SPOC	120	0.622	-	-	2600	2519	3
2MASSJ02484100-1651216	T-31/2020/SPOC	120	-	-	-	2600	2519	3.9
2MASSJ22264440-7503425	T-27/2020/SPOC	120	0.678	-	-	2500	2462	10.4
2MASSJ03061159-3647528	T-31/2020/SPOC	120	0.294	-	-	2500	2462	8.4
2MASSJ23312174-2749500	T-29/2020/SPOC	120	0.431	0.4304	12	2500	2462	8.2



Table 6: Details presented in this table are used to determine the age (last column) of Lee et al. (2010) sources. The coordinates RA, DEC and J,H,K magnitudes are taken from SIMBAD and all other parameters taken from Gaia Data Release 3 (Gaia Collaboration et al., 2022).

Source Name	RA (hh:mm:ss)	DEC (dd:mm:ss)	J	H	K	<i>g</i>	<i>bp</i>	<i>rp</i>	Proper motion in RA (mas year <sup>-1</sup> )	Proper motion in DEC (mas year <sup>-1</sup> )	Radial velocity (km s <sup>-1</sup> )	Parallax (mas)	Age (Gyr)
G 99-049	06 00 03.50	+02 42 23.59	6.905	6.308	6.042	9.901	11.545	8.654	309.1462 ± 0.0340	-40.3684 ± 0.0241	29.9568 ± 0.1742	192.0135 ± 0.0310	-
LHS 1723	05 01 57.42	-06 56 46.37	7.617	7.065	6.736	10.649	12.413	9.380	-551.7464 ± 0.0265	-533.6482 ± 0.0207	42.2863 ± 0.1750	186.0466 ± 0.0277	-
L 449-1	05 17 22.90	-35 21 54.65	7.400	6.854	6.558	10.349	11.932	9.121	-219.3826 ± 0.3094	-166.4681 ± 0.3317	-1.9771 ± 1.0568	85.4519 ± 0.2898	4.462 ± 2.904
GJ 1224	18 07 32.83	-15 57 47.06	8.639	8.085	7.827	11.863	13.780	10.560	-618.4062 ± 0.0333	-347.0067 ± 0.0269	-33.2189 ± 0.4677	125.4509 ± 0.0306	-
GL 285	07 44 40.17	+03 33 08.87	6.581	6.005	5.698	9.692	11.417	8.420	-347.7816 ± 0.0400	-445.7018 ± 0.0249	25.7171 ± 0.1962	166.9769 ± 0.0343	-
2MASS J1013426-275958	10 13 42.60	-27 59 58.63	12.261	11.626	11.252	15.837	18.051	14.444	-70.9721 ± 0.1076	-38.9926 ± 0.0877	-	24.3810 ± 0.1047	6.592 ± 3.504
GJ 1156	12 18 59.39	+11 07 33.77	8.525	7.880	7.570	11.926	14.100	10.567	-1269.7707 ± 0.0555	203.4441 ± 0.0333	-	154.6999 ± 0.0445	-
GJ 1154A	12 14 16.54	+00 37 26.36	8.456	7.860	7.540	11.829	13.859	10.491	-951.3357 ± 0.0564	-284.0494 ± 0.0389	-	123.6430 ± 0.0449	-
DENIS-P J213422.2-431610	21 34 22.29	-43 16 10.64	10.690	10.035	9.685	14.275	16.580	12.896	147.0431 ± 0.0296	-793.7512 ± 0.0282	-	59.0205 ± 0.0333	-
2MASS J02591181+0046468	02 59 11.81	+00 46 46.85	11.725	11.129	10.863	14.901	16.803	13.604	176.5674 ± 0.0381	-42.4316 ± 0.0331	34.4131 ± 5.1623	22.4993 ± 0.0363	-
2MASS J02534448-7959133	02 53 44.47	-79 59 13.26	11.336	10.740	10.379	15.051	17.619	13.632	77.2420 ± 0.0525	84.2326 ± 0.0513	-	57.2108 ± 0.0378	6.933 ± 5.093
2MASS J00244419-2708242	00 24 44.17	-27 08 25.26	9.254	8.547	8.241	13.143	15.553	11.587	-92.7389 ± 0.1108	695.9562 ± 0.1171	-28.9832 ± 0.7666	129.3167 ± 0.1256	0.831 ± 4.808
2MASS J00045753-1709369	00 04 57.54	-17 09 36.95	10.997	10.455	10.084	14.582	16.969	13.196	144.7759 ± 0.0426	-8.9428 ± 0.0341	-	58.6246 ± 0.0492	5.048 ± 2.755
2MASS J20021341-5425558	20 02 13.44	-54 25 55.90	11.621	11.035	10.644	15.487	18.355	14.037	61.5745 ± 0.0455	-365.2540 ± 0.0410	-	55.5167 ± 0.0526	-
LP 844-25	08 53 56.35	-24 46 56.44	12.386	11.879	11.571	15.796	18.228	14.408	611.5040 ± 0.0519	157.3040 ± 0.0519	-	38.8220 ± 0.0548	0.609 ± 0.168
2MASS J16142520-0251009	16 14 25.19	-02 51 00.75	11.303	10.683	10.280	15.223	18.242	13.752	-7.8084 ± 0.0827	367.4055 ± 0.0610	-	68.9493 ± 0.0835	-
2MASS J21322975-0511585	21 32 29.76	-05 11 59.02	11.423	10.730	10.379	15.095	17.596	13.692	115.9966 ± 0.0524	-341.4850 ± 0.0354	-	49.7147 ± 0.0476	0.22 ± 6.675
2MASS J23373831-1250277	23 37 38.34	-12 50 28.36	11.462	10.830	10.452	15.320	17.780	13.803	192.5646 ± 0.4121	-305.8209 ± 0.3055	-	37.4154 ± 0.3504	0.129 ± 0.037
2MASSW J1012065-304926	10 12 06.48	-30 49 26.32	12.223	11.601	11.179	16.272	19.355	14.795	-142.4917 ± 0.0646	36.0642 ± 0.0822	-	44.2132 ± 0.0656	-
LP 731-47	11 06 56.91	-12 44 02.73	11.786	11.188	10.792	15.942	18.711	14.352	-358.6362 ± 0.0262	22.2501 ± 0.4898	-	41.9403 ± 0.0676	0.193 ± 0.047
2MASS J23155449-0627462	23 15 54.50	-06 27 46.42	11.111	10.567	10.228	14.795	17.338	13.383	315.1335 ± 0.0340	-44.9079 ± 0.0385	-	59.6358 ± 0.0481	1.927 ± 0.022
2MASS J20424514-0500193	20 42 45.17	-05 00 19.17	11.449	10.871	10.539	15.175	17.867	13.746	241.0537 ± 0.0507	116.9923 ± 0.0369	-17.6063 ± 2.9483	1.4739 ± 0.6710	1.329 ± 0.361
GJ 3622	10 48 13.61	-11 20 09.61	8.857	8.263	7.930	12.837	15.941	11.360	579.0187 ± 0.0658	-1530.0765 ± 0.0576	-	219.3302 ± 0.0602	-
2MASS J05023867-3227500	05 02 38.68	-32 27 50.10	12.443	11.814	11.439	16.222	18.821	14.786	55.8091 ± 0.0473	-164.1750 ± 0.0611	-	34.1292 ± 0.0504	5.634 ± 2.441
2MASS J02141251-0357434	02 14 12.56	-03 57 43.58	10.481	9.858	9.485	14.148	16.666	12.741	509.6377 ± 0.0507	-155.8128 ± 0.0428	-	80.0548 ± 0.0626	-
2MASS J10031918-0105079	10 03 19.15	-01 05 08.00	12.327	11.667	11.236	16.527	19.746	15.012	-498.7060 ± 0.0920	46.9003 ± 0.1023	-	50.1379 ± 0.0950	8.147 ± 2.340
2MASS J13092185-2330350	13 09 21.85	-23 30 35.74	11.785	11.082	10.669	16.120	19.467	14.592	15.7296 ± 0.1066	-383.7718 ± 0.0727	-	66.6038 ± 0.0976	-
2MASSW J1032136-420856	10 32 13.68	-42 08 56.94	12.888	12.211	11.829	17.115	20.206	15.598	91.5176 ± 0.0702	-159.2972 ± 0.0871	-	39.3327 ± 0.0922	2.375 ± 0.000
2MASSW J1420544-361322	14 20 54.47	-36 13 22.26	11.477	10.843	10.420	16.146	18.998	14.144	-	-	-	-	-
2MASS J09522188-1924319	09 52 21.88	-19 24 32.20	11.865	11.256	10.869	15.735	18.468	14.292	-73.0006 ± 0.1044	-99.4799 ± 0.1032	-	35.3239 ± 0.1038	-
2MASS J04291842-3123568	04 29 18.46	-31 23 56.74	10.874	10.211	9.770	15.028	17.556	13.403	65.8199 ± 0.1493	99.5806 ± 0.1636	-	58.7935 ± 0.1420	11.108 ± 5.887
2MASS J23062928-0502285	23 06 29.36	-05 02 29.03	11.354	10.718	10.296	15.623	19.006	14.104	930.7875 ± 0.0868	-479.0375 ± 0.0705	-	80.2123 ± 0.0716	-
2MASS J03313025-3042383	03 31 30.25	-30 42 38.82	11.360	10.700	10.264	15.628	19.029	14.109	51.8694 ± 0.0408	-403.0845 ± 0.0554	-	79.9468 ± 0.0556	-
2MASS J04351612-1606574	04 35 16.14	-16 06 57.21	10.406	9.779	9.352	14.607	17.921	13.099	160.0832 ± 0.1716	315.1396 ± 0.1683	-	94.3054 ± 0.2099	-
2MASS J06572547-4019134	06 57 25.43	-40 19 13.76	12.728	12.132	11.667	17.796	20.610	15.586	-107.7470 ± 0.1924	64.3169 ± 0.2046	-	29.1861 ± 0.1660	-
2MASS J05173766-3349027	05 17 37.69	-33 49 03.09	12.004	11.317	10.832	16.484	20.002	14.942	445.8376 ± 0.0798	-331.4433 ± 0.0943	-	59.4702 ± 0.0779	-
2MASS J19165762+0509021	19 16 57.61	+05 09 01.60	9.908	9.226	8.765	14.303	17.746	12.775	-598.7613 ± 0.0717	-1366.0635 ± 0.0650	-	168.9537 ± 0.0668	-
2MASS J22062280-2047058	22 06 22.82	-20 47 06.59	12.370	11.684	11.315	16.918	20.013	15.095	-	-	-	-	8.038 ± 4.052
2MASS J02484100-1651216	02 48 40.99	-16 51 22.12	12.551	11.872	11.422	16.848	20.102	15.318	-33.1201 ± 0.1276	-288.8480 ± 0.1536	-	44.6207 ± 0.1262	8.264 ± 3.51
2MASS J20370715-1137569	20 37 07.15	-11 37 57.34	12.272	11.629	11.257	16.389	19.627	14.879	-2.2340 ± 0.1121	-379.1496 ± 0.0917	-	46.6595 ± 0.1034	-
2MASS J22264440-7503425	22 26 44.41	-75 03 42.53	12.353	11.696	11.246	16.798	20.282	15.239	58.7394 ± 0.0838	11.7791 ± 0.0923	-	42.6368 ± 0.0779	-
2MASS J03061159-3647528	03 06 11.59	-36 47 52.85	11.690	11.068	10.631	15.994	19.534	14.460	-172.1654 ± 0.0497	-669.2439 ± 0.0576	-	75.4184 ± 0.0580	-
2MASS J23312174-2749500	23 31 21.74	-27 49 49.60	11.646	11.055	10.651	15.870	19.514	14.347	90.3750 ± 0.0752	745.2837 ± 0.0715	-	73.3785 ± 0.0770	-